

# Quantitative Analysis of Semiconductor Nanocrystal Ensemble Optical Extinction

Corey M. Staller<sup>†</sup>, Ankit Agrawal<sup>†</sup>, Stephen L. Gibbs<sup>†</sup>, Camila A. Saez Cabezas<sup>†</sup>, Robert W. Johns<sup>||,†</sup>, Delia J. Milliron<sup>\*,†</sup>

<sup>†</sup>McKetta Department of Chemical Engineering, University of Texas at Austin, Austin, Texas, 78712-1589, United States

<sup>||</sup> Department of Chemistry, University of California, Berkeley, Berkeley, California 94720, USA

Corresponding Author

E-mail: [milliron@che.utexas.edu](mailto:milliron@che.utexas.edu)

Telephone: (512)232-5702

**ABSTRACT:** The optical extinction coefficients of localized surface plasmon resonance (LSPR) in doped semiconductor nanocrystals (NCs) have intensities determined by the free charge carrier concentration and the mechanisms for damping the oscillation of those free carriers. We investigate the dependence of the extinction coefficient of tin-doped indium oxide (ITO) NCs on size and dopant concentration and find extinction coefficients as high as  $56.5 \mu\text{m}^{-1}$  in the near infrared for 7.5 atomic% Sn 20 nm diameter ITO NCs. We demonstrate a new fitting procedure for the optical extinction of an ensemble of well-dispersed NCs that accounts for NC size heterogeneity, electron concentration heterogeneity, surface scattering, and near-surface electron depletion due to surface states. The heterogeneous ensemble Drude approximation (HEDA) model utilizes the same number of variables as previous models and fits data as well or better while using inputs and fitting parameters that are described by physical phenomena. The model improves the understanding of free carrier motion in doped semiconductor NCs by more accurately extracting carrier concentration and carrier damping. The HEDA model captures individual NC optical properties and their contributions to the ensemble spectra. We find the peak extinction coefficient of an average NC varies linearly with the product of electron accessible volume fraction and electron concentration, normalized by damping.

**KEYWORDS:** Nanocrystals, Tin-doped Indium Oxide, Extinction Coefficient, Surface Scattering, Polydispersity, Depletion Layer

Metal nanoparticles (NPs) and semiconductor nanocrystals (NCs) with high free charge carrier concentration are widely studied for their distinctive optical properties. Of principal importance is their strong, frequency-dependent polarizability arising from the oscillation of free charge carriers in response to incident electromagnetic radiation, known as a localized surface plasmon resonance (LSPR). The efficient extinction of incident radiation by nanoscale materials makes plasmonic NCs ideal candidates for use in electrochromic windows<sup>1-3</sup>, sensors<sup>4-9</sup>, and photothermal theranostics.<sup>10-15</sup> In contrast to metal NPs, doped semiconductor NCs derive free charge carriers from charge-compensated crystal defects resulting in carrier concentrations orders of magnitude lower, placing the LSPR frequency ( $\omega_{\text{LSPR}}$ ) in the infrared (IR). The carrier concentration can easily be modulated synthetically through tuning dopant concentration and post-synthetically by imposing an electrochemical bias or through photoelectrochemical charging.<sup>1,16-18</sup> Unable to significantly modulate carrier concentration, metal NP LSPR frequency is primarily tuned by manipulating particle size and geometry.<sup>19-22</sup> The capability of tuning carrier concentration in semiconductor NCs allows IR LSPR tunability across a range of NC sizes, while Au NPs require sizes  $>200$  nm or complex geometries to achieve IR attenuation.<sup>19,23-29</sup>

While several studies have investigated Au NP absorption coefficients, doped semiconductor NC absorption coefficients, particularly for doped metal oxides, are not yet established.<sup>30,31</sup> The applications mentioned above require high absorption coefficient materials to be feasible and given that doped metal oxide NCs show promise as strong IR absorbers, it is important to quantitatively investigate their optical extinction properties.

The far-field extinction spectrum of an ensemble of plasmonic NCs is influenced by a variety of factors. Of principal importance are damping processes that broaden the LSPR of individual NCs, broadening due to ensemble NC heterogeneity (heterogeneous broadening), and electron concentration. Individual NC damping is a direct measure of the electron mobility within a NC, which is dependent on the electron mean free path. The mean free path has been proposed to be dominated by surface scattering in nanostructures with one or more dimensions smaller than the bulk mean free path.<sup>32</sup> Size-dependent damping consistent with free electron surface scattering was observed by Wokaun et al. in Ag NPs<sup>33</sup> and Link et al. in Au NPs.<sup>34</sup> The prominence of surface scattering emphasizes the importance of accounting for near-surface depletion regions. When free electrons are depleted from the NC in favor of filling empty surface states, a thin outer shell becomes devoid of free carriers, which effectively shrinks the volume accessible to conduction electrons. Zandi et al. and Agrawal et al. observed a strong effect of near-surface depletion regions on the optical properties of tin-doped indium oxide (ITO) NC films and dispersions.<sup>35,36</sup>

Current optical models frequently convolute individual NC damping and heterogeneous broadening into a single damping term, leading to misinterpretation of material electronic properties. Despite the rather narrow size distributions achieved by recent synthetic developments, size polydispersity is still often nearly 10%.<sup>37,38</sup> When surface scattering is prominent, a size distribution within an ensemble of NCs causes a distribution of intra-NC electron mobility due to variations in surface scattering, resulting in heterogeneous peak broadening. Additionally, Johns et al. showed striking variability in absorption peak energy and linewidth of single NC absorption spectra within populations of aluminum-doped zinc oxide and ITO NCs.<sup>39</sup> These results support the existence of significant carrier concentration polydispersity even among a group of NCs synthesized in the same batch, which results in heterogeneous broadening. Although many factors have been identified which influence the absorption spectrum of doped semiconductor NCs, a quantitative, physics-based model that captures each of these contributions has not yet been reported.

Herein, we investigate the influence of NC size and dopant concentration on the extinction peak energy, lineshape, and intensity for doped semiconductor NCs. We use ITO NCs of varying dopant concentrations and sizes as a model system. Using quantitative analysis of optical spectra, we find the ITO NC extinction coefficient correlates strongly with NC size and dopant concentration. We suggest these correlations result from changes in electron concentration and damping due to differences in dopant activation, surface scattering, and near-surface depletion. We present a model for fitting optical spectra of NC ensembles that captures the effects of these factors. This procedure uses only well-known material constants and routinely measured NC physical properties to fit for a distribution of NC properties that cannot be easily measured directly, namely carrier concentration, carrier concentration polydispersity, and near-surface depletion width. By analyzing the far-field response as a sum of contributions from individual NCs, the ensemble fit enables analysis of physical properties for the average NC within an ensemble. We find the extinction coefficient of an average NC varies linearly with  $f_e \frac{\omega_p^2}{\Gamma}$ . The previously used model, the simple Drude model, underestimates the optical conductivity of NCs due to the convolution of individual NC damping and heterogeneous broadening contributions.

## Extinction Coefficient of ITO NC Ensembles

The Beer-Lambert Law defines the efficiency with which a material extinguishes light of a particular wavelength. The Beer-Lambert Law is considered from two perspectives. The first is within a homogeneous framework, represented as

$$A = \frac{\epsilon f_V l}{\ln(10)} \quad \text{Equation 1}$$

where  $A$  is the measured extinction in base 10 log scale, also referred to as optical density (OD),  $f_V$  is the volume fraction of the absorbing material,  $l$  is the pathlength through the sample,  $\ln(10)$  is included to convert extinction to natural log scale, and  $\epsilon$  is the extinction coefficient ( $\mu\text{m}^{-1}$ ). While the extinction coefficient is not useful for probing the charge-carrier physics of systems with heterogeneous broadening, it is a critical engineering parameter for optical applications.

Two series were prepared to investigate the role of NC size and dopant concentration on the optical properties of ITO NCs: a doping series from 0 to 7.5 atomic% Sn at 20 nm diameter and a size series from 6.5 to 20 nm diameter at 5 atomic% Sn. To investigate the optical extinction coefficient of ITO NCs, optical spectra were taken of NC dispersions at various NC volume fractions. Figure 1a shows a representative dilution series at 5 different dilution factors ranging from 840x to 160x relative to a 34 mg/mL stock solution. Accurate calculation of NC extinction coefficients requires the absence of NC-NC interactions such as NC-NC coupling or aggregation.<sup>32</sup> This condition can be tested by varying the volume fraction of NCs in solution and inspecting extinction spectra for any response other than a linear dependence of extinction on NC concentration across all wavelengths. When normalized, spectra of all dilutions overlap nearly perfectly (Figure 1b). The extinction at  $\omega_{\text{LSPR}}$  is shown to be linear with NC volume fraction (Figure 1c). These data verify that NC-NC interactions are absent in NC dispersions utilized in these studies. The extinction coefficient at  $\omega_{\text{LSPR}}$  is calculated from the slope of extinction versus NC volume fraction in Figure 1c.

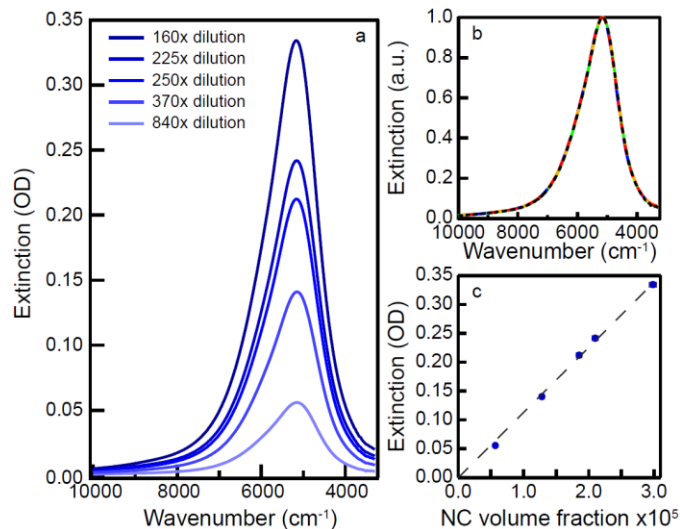


**Figure 1.** Extinction coefficient dilution series (a), normalized dilution spectra (b), and linear fit to extinction v. NC volume fraction at  $\omega_{\text{LSPR}}$  (c) for 6 atomic% Sn doped 20 nm ITO.

Figure 2a shows the quantitative extinction spectrum of all samples in a series of dopant concentrations. Increasing dopant concentration manifests in a significant blue shift and increased intensity of the ITO LSPR peak, indicating an increase in carrier concentration. Inspection of Figure 2b shows an approximately linear relationship between extinction coefficient and dopant concentration up to about 5 atomic% Sn. The saturation of the trend with further doping agrees with the dopant compensation region in the Brouwer diagram of ITO at high Sn concentration wherein it becomes favorable for the positive charge associated with  $Sn_{In}^{\bullet}$  defect to be compensated by forming a neutral defect cluster,  $2Sn_{In}^{\bullet}O_i''$ .<sup>40,41</sup> This interpretation is supported by an increase of the optical band gap with dopant concentration, consistent with increasing electron concentration, i.e. the Burstein-Moss effect (Figure S7).

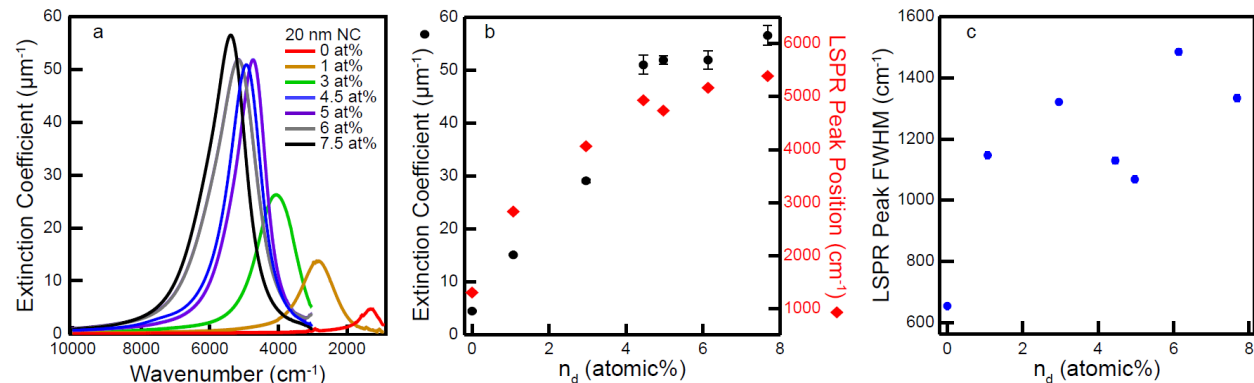


**Figure 2. Dopant concentration series** quantitative LSPR extinction spectra (a), extinction coefficient and LSPR peak energy v. dopant concentration,  $n_d$ , (b), and LSPR peak full-width at half-maximum (FWHM) v. dopant concentration (c).

LSPR peak energy rapidly increases with dopant concentration under 4.5 atomic% Sn. In the absence of near-surface depletion regions, the LSPR peak energy is expected to blue shift proportionally with the square root of electron concentration. We observe an even more rapid blue shift of the LSPR with dopant concentration, which can be ascribed to the presence of near-surface depletion regions, as discussed below. The LSPR peak full-width at half-maximum (FWHM) trends upward with increased dopant concentration (Figure 2c), suggesting stronger damping and lower electronic mobility at higher dopant concentration as may be expected. However, as detailed below, FWHM of such ensemble spectra alone is not sufficient to draw conclusions regarding damping physics as it convolutes contributions from single NC damping and heterogeneous broadening.

Figure 3a shows the quantitative extinction spectra of each sample in the size series. The LSPR intensity increases with NC radius as predicted in Au NPs.<sup>42</sup> While the extinction coefficient at  $\omega_{\text{LSPR}}$  of Au NPs is approximately linear with NP diameter, the relationship for the ITO NCs measured here is significantly more complicated. Additionally, the LSPR peak energy for ITO NCs tends to blue shift with increasing NC radius while Au NPs display no size dependence below 4 nm diameter and the opposite trend at larger sizes.<sup>19,42</sup> These correlations are attributed, in part, to an increase of electron concentration at increased NC size and are supported by an increase of the optical band gap with NC radius at constant 5 atomic% Sn (Figure S7). The LSPR peak shape narrows with NC radius, which is qualitatively consistent with surface scattering impacting plasmon damping, as will be elaborated below.

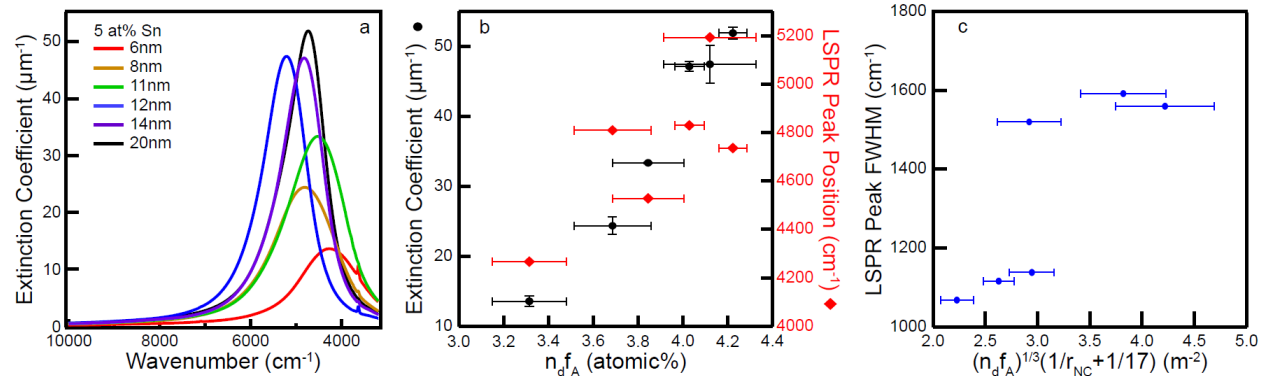


**Figure 3. Size series** quantitative LSPR extinction spectra (a), extinction coefficient and LSPR peak energy v. activated dopant concentration (b), and LSPR peak full-width at half-maximum (FWHM) v. theoretical total damping (c).

The extinction coefficients at the LSPR peak of ITO NCs reported here range from 4.5  $\mu\text{m}^{-1}$  at 1300  $\text{cm}^{-1}$  for 20 nm undoped indium oxide NCs to 56.5  $\mu\text{m}^{-1}$  at 5289  $\text{cm}^{-1}$  for 20 nm 7.5 atomic% Sn ITO NCs. ITO NCs have a phenomenally high extinction coefficient in the IR, especially when compared to other IR absorbing materials. Common IR absorbing or scattering materials such as Au nanostructures ( $\epsilon_{sca} = 35.5 \mu\text{m}^{-1}$  at 8620  $\text{cm}^{-1}$ )<sup>19</sup>, Cu<sub>2-x</sub>Se NCs ( $\epsilon_{abs} = 23.5 \mu\text{m}^{-1}$  at 9399  $\text{cm}^{-1}$ )<sup>43</sup>, and the first exciton peak of 5.5 nm PbSe QDs ( $\epsilon_{abs} = 12.7 \mu\text{m}^{-1}$  at 6250  $\text{cm}^{-1}$ )<sup>44</sup> attenuate IR light less efficiently than 20 nm 4.5 atomic% Sn ITO NCs. To our knowledge, the ITO NCs reported here have the highest extinction coefficient of IR absorbing material reported. Remarkably, ITO NCs have extinction coefficient quite close to the absorption coefficient of spherical Au NPs of diameter 4 – 20 nm (34.0 – 73.7  $\mu\text{m}^{-1}$ ) despite having a peak much lower in energy.<sup>19,34,42</sup> Alternative extinction coefficient units for these samples are shown in Table S1 for comparison.

## Theory

Metal oxide surfaces are passivated by adsorbed water species, including surface hydroxyls, that create a density of electronic states near the NC surface. When these surface states are within the optical band gap they cause a decreased electron concentration near the NC surface, known as a depletion region (Figure 4ai).<sup>35–37</sup> Due to the buildup of electrostatic potential, depletion regions near the NC surface decrease the fraction of the NC volume accessible to conduction electrons,  $f_e$ . The radius of the spherical volume accessible to conduction electrons is  $f_e^{1/3} r_{NC}$ , where  $r_{NC}$  is the physical NC radius. This decreased radius is referred to as the electron accessible radius. Aside from decreasing the volume accessible to electrons, near-surface depletion creates a pseudo-core-shell geometry where the NC is composed of a plasmonic core with an electron-deficient dielectric shell (Figure 4aii). This geometry requires a modification to the dielectric function of these materials to successfully model their optical response.

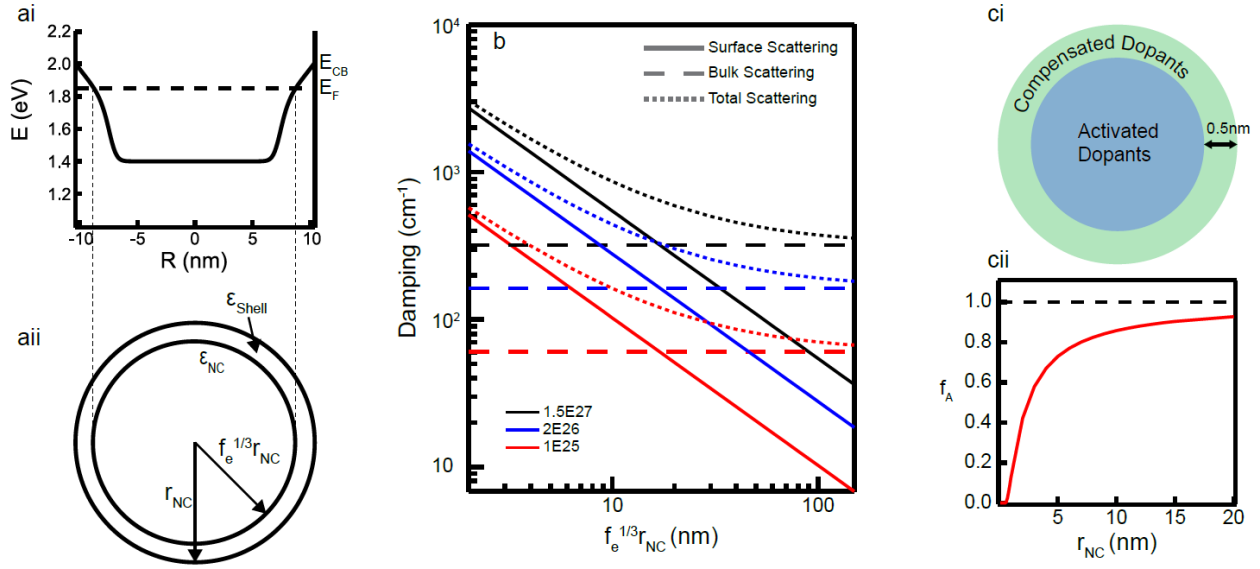


**Figure 4. Theoretical concepts.** NC with surface depletion band profile (ai) and schematic (aia), damping due to surface scattering, bulk scattering, and total scattering for three different electron concentrations as a function of the radius of the plasmonically active core (b), and NC surface dopant compensation schematic (ci) and fractional activation (cii).

The LSPR line width of a single spherical NC is described by the damping constant, which is the rate at which conduction electrons scatter. While damping is often used as a fitting parameter, it can be calculated from the Drude conductivity as<sup>34,45</sup>

$$\Gamma = \frac{(3\pi^2)^{\frac{1}{3}} \hbar}{m_e^*} n_e^{\frac{1}{3}} \left( \frac{1}{l_{MFP}} \right) \quad \text{Equation 2}$$

where  $\hbar$  is Planck's constant,  $m_e^*$  is the effective electron mass,  $n_e$  is the electron concentration, and  $l_{MFP}$  is the electron mean free path. For NCs of radius comparable to or less than the material bulk mean free path, surface scattering influences the overall mean free path of NC conduction electrons.<sup>34,45,46</sup> Surface scattering is included in the mean free path using an assumption of surface scattering being a specular scattering event and applying Matthiessen's rule as<sup>32,46</sup>

$$\frac{1}{l_{MFP}} = \left( \frac{1}{\frac{4}{3} r_{NC} f_e^{\frac{1}{3}}} + \frac{1}{l_{bulk}} \right) \quad \text{Equation 3}$$

where  $l_{bulk}$  is the bulk mean free path (17 nm for ITO).<sup>47</sup> The bulk mean free path is assumed to be constant based on work by Frank and Kostlin.<sup>40</sup> The surface damping contribution, bulk damping contribution, and total damping are plotted against the electron accessible radius for a range of electron concentrations in Figure 4b. Inspection of the total damping curve shows the dominance of surface scattering when the electron accessible radius is smaller than the bulk mean free path. Surface scattering becomes negligible at 10x the bulk mean free path, 170 nm for ITO, which is larger than typical NC radii. Thus, typical size polydispersity of about 10% leads to a significant variance between individual NCs in surface damping, emphasizing the need to consider size polydispersity when extracting electronic properties from ensemble LSPR spectra.

When dopants are preferentially distributed in the near-surface region, NCs exhibit lower dopant activation, which has strong implications for electron concentration.<sup>48</sup> We assume, at modest overall dopant concentrations, full activation of dopants outside of the near-surface region. The thickness of the deactivation layer is assumed to be 0.5 nm, half of an indium oxide unit cell, as shown in Figure 4ci.<sup>40</sup> The overall fraction of activated dopants,  $f_A$ , in a uniformly doped NC is expected to be size-sensitive as a result of the deactivation layer (Figure 4cii). The effect of decreased dopant activation in the near-surface region of NCs is evident in the optical spectra of ITO NCs of varying size (Figure 3a). The activated dopant concentration is defined as  $n_d f_A$  where  $n_d$  is the dopant concentration, determined quantitatively by elemental analysis. The LSPR peak energy and extinction coefficient trends approximately linearly with the activated dopant concentration (Figure 3b). LSPR peak energy trends upward with activated dopant concentration.

When measuring the optical response of an ensemble of NCs, both size polydispersity and carrier concentration variability will contribute to heterogeneous broadening of the LSPR peak. When not considered, heterogeneous broadening will lead to misattributing size heterogeneity and carrier concentration heterogeneity to a larger intrinsic damping constant, deduced from the peak width. An alternative framework for the extinction coefficient previously used in the Beer-Lambert law is derived to account for near-surface depletion, surface scattering, and NC heterogeneity. The new model is termed the Heterogeneous Ensemble Drude Approximation (HEDA) wherein size heterogeneity and electron concentration heterogeneity are modeled using Gaussian distributions. To do this, we construct a two-parameter probability density function with a 41x41 data point mesh (Figure S1). The extinction of each of the 1681 points is probability-weighted and summed to give the ensemble extinction. The complex dielectric function,  $\varepsilon_{NCij}(\omega)$ , of each spherical electron cloud with radius,  $r_i$ , and electron concentration,  $n_{e_j}$ , is expressed using the Drude-Lorentz model

$$\varepsilon_{NCij}(\omega) = \varepsilon_\infty - \frac{\omega_{p_j}^2}{\omega^2 + i\omega\Gamma_{ij}} \quad \text{Equation 4}$$

where  $\varepsilon_\infty$  is the material high-frequency dielectric constant,  $\Gamma_{ij}$  is the damping constant, and  $\omega_{p_j}$  is the plasma frequency. The damping constant,  $\Gamma_{ij}$ , is defined using Equations 2 and 3 as

$$\Gamma_{ij} = \frac{(3\pi^2)^{\frac{1}{3}} \hbar}{m_e^*} n_{e_j}^{\frac{1}{3}} \left( \frac{1}{\frac{4}{3} r_{NCi} f_e^{\frac{1}{3}}} + \frac{1}{l_{bulk}} \right) \quad \text{Equation 5}$$

The LSPR peak FWHM trends toward larger values as NC radius decreases for the size series (Figure 3c). The impact of size-dependent surface scattering on LSPR peak FWHM is convoluted with the size-dependence of dopant activation discussed above. Despite this, smaller NCs exhibit significantly larger values of FWHM.

$\omega_{p_j}$  is defined as

$$\omega_{p_j} = \sqrt{\frac{q^2 n_{e_j}}{\varepsilon_0 m_e^*}} \quad \text{Equation 6}$$

where  $q$  is the electron charge and  $\varepsilon_0$  is the permittivity of vacuum. The presence of depletion near NC surfaces necessitates a Maxwell-Garnett effective medium approximation (EMA) to define the dielectric function of a core-shell NC,  $\varepsilon_{CSij}$ , as

$$\varepsilon_{csij}(\omega) = \varepsilon_{shell} \left( \frac{(\varepsilon_{NCij} + 2\varepsilon_{shell}) + 2f_e(\varepsilon_{NCij} - \varepsilon_{shell})}{(\varepsilon_{NCij} + 2\varepsilon_{shell}) - f_e(\varepsilon_{NCij} - \varepsilon_{shell})} \right) \quad \text{Equation 7}$$

where  $\varepsilon_{shell}$  is the dielectric function of the depleted shell. It is noted that the EMA converges to  $\varepsilon_{NCij}(\omega)$  when  $f_e = 1$  and is therefore a general solution. In systems of non-interacting spheres the absorption cross section of a given particle,  $\sigma_{absij}$ , is defined by Mie theory as

$$\sigma_{absij}(\omega) = 8\pi^2 r_{NCi}^3 \omega \sqrt{\varepsilon_m} \text{Imag} \left\{ \frac{\varepsilon_{csij}(\omega) - \varepsilon_m}{\varepsilon_{csij}(\omega) + 2\varepsilon_m} \right\} \quad \text{Equation 8}$$

where  $\varepsilon_m$  is the dielectric constant of the medium. For NCs smaller than 5% the wavelength of incident light, optical scattering is negligible and extinction is assumed to be entirely due to absorption.<sup>49</sup> This assumption holds up to at least 150 nm diameter for ITO NCs. The absorption cross section for each of the 1681 points is probability-weighted and summed to give the effective absorption cross section for the ensemble,  $\sigma_{abs}^{eff}$ , as

$$\sigma_{abs}^{eff} = \sum_i^m \sum_j^n \left( \sigma_{absij}(\omega) p_{n_{e_j}} p_{r_{NCi}} \Delta n_e \Delta r_{NC} \right) \quad \text{Equation 9}$$

where  $p_{n_{e_j}}$  and  $p_{r_{NCi}}$  are the probabilities of  $n_{e_j}$  and  $r_{NCi}$ , respectively,  $\Delta n_e$  and  $\Delta r_{NCi}$  are the step sizes for  $n_e$  and  $r_{NC}$ , respectively, and  $m$  and  $n$  are the mesh dimensions (41 here). The effective absorption cross section of the ensemble is then plugged into the Beer-Lambert law,

$$A = \frac{f_V l}{\ln(10)V} \sigma_{abs}^{eff} \quad \text{Equation 10}$$

where  $V$  is the probability normalized volume of a NC, defined as

$$V = \sum_i^m \sum_j^n \left( \frac{4}{3} \pi r_{NCi}^3 p_{n_{e_j}} p_{r_{NCi}} \Delta n_e \Delta r_{NC} \right) \quad \text{Equation 11}$$

Simulations of quantitative single NC extinction spectra using Equations 4-11 with varying electron concentration, size, and near-surface depletion are shown in Figure S2.

### Extracting Reliable Material Parameters with the HEDA Model

The previous section exemplifies the type of conclusions that can be drawn from ensemble measurements of plasmonic NCs. General trends in extinction with size and doping can be determined, but their interpretation in terms of fundamental material properties is clouded by the contributions of size and carrier concentration polydispersity. Doping and size series optical extinction spectra were fit and analyzed using the simple Drude approximation (SDA) and HEDA models. Previous SDA model fitting procedures require the input of pathlength and material constants that are used to fit for volume fraction, damping constant, and plasma frequency. These fitting procedures often yield a volume fraction that is not physically reconcilable with the measured sample, but instead acts as a correction factor that scales the fitted extinction intensity. The model presented here, in addition to the basic inputs above, takes as fixed inputs the NC radius mean value, radius standard deviation, and measured volume fraction, all of which are directly measured on our experimental samples. The fitting procedure outputs are the electron concentration mean value its standard deviation, and the effective non-depleted volume fraction. This represents an identical number of fit variables to previous SDA



fitting procedures, but provides far richer and more accurate information regarding the properties of the NC ensemble.

The HEDA model fit is compared to the SDA model using volume fraction as a fitting parameter and to the SDA with volume fraction fixed to the measured value. Examples of fits to experimental data are shown in Figure 5a and all fitted spectra are shown in Figure S8 and are summarized for the dopant concentration (Table S2) and NC size (Table S3) series. Comparing the fits in Figure 5a reveals shortfalls of the SDA model: the inability to fit peak shape, peak intensity, and converge on the measured volume fraction consistently (Figure S8). These discrepancies arise because the SDA does not account for near-surface depletion and the associated core-shell EMA, and it incorrectly ascribes heterogeneous broadening to homogeneous broadening within a single damping term.<sup>50</sup> When the volume fraction is fixed to the measured value, the SDA is unable to simultaneously fit peak intensity and lineshape, resulting in poor fits as shown in Figure 5a.

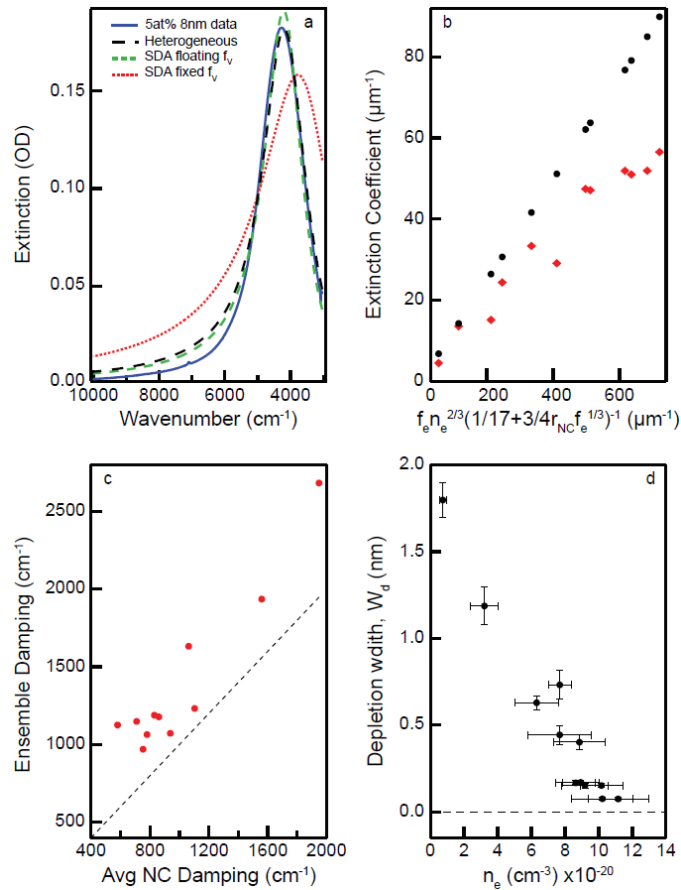


**Figure 5. Fitting extinction spectra.** Simple Drude Approximation (SDA) with a floating NC volume fraction, SDA with measured NC loading, and heterogeneous Drude (HEDA) fits to extinction data for 5 at% 8 nm ITO (a), average NC (black) and ensemble (red) extinction coefficient dependence on plasma frequency and damping (b), SDA ensemble damping constant compared to the HEDA-derived damping (c), and near-surface depletion width,  $W_d$ , versus electron concentration (d). Error bars in (d) represent the calculated error based on propagation of NC size standard deviation (y-axis) and fitted electron concentration standard deviation (x-axis) in the ensemble for each sample.

The HEDA model enables the analysis of the properties of the average NC in an ensemble by deconvoluting single NC properties from heterogeneous broadening. The extinction spectrum of the average NC in an ensemble is simulated using the mean NC radius and HEDA model values for mean electron concentration and electron accessible volume fraction (Figure 5b, S9). Single NC extinction spectra exhibit a significantly higher extinction coefficient than the corresponding ensemble. This difference arises due to the distribution of peak locations, intensities, and widths that broaden the absorption peak of the ensemble and reducing the peak intensity. Additionally, the extinction coefficient of an average NC increases linearly with  $f_e \frac{\omega_p^2}{\Gamma}$ . This trend is in agreement with the analytical solution of Mie theory at the LSPR peak when  $\omega_p \gg \Gamma$ , as shown in SI Text 1. This relationship reveals the key to achieving high absorbing NC ensembles in the IR as monodisperse NCs of large radius and high dopant concentration.

Fitting LSPR ensemble absorption with SDA is a common method for assessing the conductivity or mobility of electrons within NCs. These properties are calculated from the fitted electron concentration and damping constant. While the SDA-derived electron concentration does not differ significantly from the average electron concentration found by fitting with HEDA model, simulating absorption spectra of average NCs reveals that single NCs exhibit a significantly reduced linewidth compared to the associated ensemble, consistent with previous experimental results.<sup>39</sup> Using SDA to represent the apparent damping of the ensemble and HEDA model to represent the average NC, Figure 5c compares apparent and intrinsic damping. The ensemble damping is 12-110% higher than the damping of an average NC in an ensemble. The overestimate of damping by the SDA results from the assumption of each NC being identical, while in reality heterogeneity substantially contributes to LSPR broadening. The overestimation of damping results in misleadingly low conductivity and mobility within the NCs and inhibits meaningful interpretation of these material properties.

One potential source of error for the HEDA model is non-physical fit parameter correlations. While the HEDA model has an identical number of free parameters as the SDA, it contains multiple broadening parameters (specifically,  $f_e$  and  $\sigma_{n_e}$ ). The depletion width of a semiconductor with a depleted surface is expected to decrease with increased ionized dopant concentration.<sup>35,37</sup> Figure 5d shows the depletion width,  $W_d = r_{NC}(1 - f_e)^{\frac{1}{3}}$ , decreases with the electron concentration of NCs in the dispersion, as expected. Here, electron concentration is considered to be representative of the ionized dopant concentration. The second fitted broadening parameter,  $\sigma_{n_e}$ , shows no correlation with the non-depleted volume fraction (Figure S10). This independence of the two primary broadening factors indicates the HEDA model is robust.

In conclusion, NC dopant concentration and size were shown to play a prominent role in determining LSPR peak energy, linewidth, and intensity. These effects are understood based on surface dopant compensation, surface scattering, and near-surface depletion. These effects were analyzed using a novel fitting procedure to account for NC size and electron concentration heterogeneities, representing a powerful tool for characterizing electronic properties of NCs. The results presented should be viewed as generally valid for doped semiconductor NCs at sizes comparable to or smaller than the material bulk mean free path. At the onset, we pointed out  $\omega_{LSPR}$  trends in opposite directions with size when comparing Au and ITO. Through our analysis, we found that larger NC radius increases electron concentration and reduces depletion width, lowering the dielectric constant of the surroundings. This effect is not absent or weak in Au owing to the very high carrier concentration, explaining the differing trends.

We have quantitatively analyzed the influence of size and dopant concentration on the LSPR of ITO NCs. NC extinction coefficient and LSPR peak position were shown to correlate with dopant concentration and size, with surface dopant compensation resulting in lower dopant activation for smaller NCs. Ensemble LSPR peak widths convolute intrinsic damping and heterogeneous broadening. In the size regime investigated here, intrinsic damping is dominated by surface scattering and heterogeneous broadening results from NC to NC variations in size and electron concentration. These results were substantiated by a physics-based LSPR peak fitting procedure that accounts for surface scattering, heterogeneity, and near-surface depletion with an identical number of fit parameters as previous models. Our results indicate synthesizing large and highly doped semiconductor NCs is an optimal strategy for achieving narrow and high extinction coefficient LSPR in the infrared, a necessary characteristic for electrochromic devices, sensors, and photothermal applications.

## Experimental Procedures

### Synthesis of ITO NCs

ITO NCs were synthesized by modification of methods published by the Hutchison group.<sup>1,2</sup> NC cores were synthesized by adding 4.7 mmol of metal precursor (In(III)acetate and Sn(IV)acetate) to 10 mL of oleic acid in a round bottom flask. This will be referred to as the precursor flask. The precursor flask is then put under vacuum and heated to 110°C for 1 hour with one pump/purge midway through the hour. The precursor flask is then put under nitrogen and heated to 150°C for 2 hours to generate In- and Sn-oleate. Concurrently, 12 mL of oleyl alcohol is put in a second round bottom flask, called the reaction flask. The reaction flask is put under vacuum and heated to 150°C for 2 hours with one pump/purge midway through. The reaction flask is then heated to 290°C under nitrogen. Once the In- and Sn-oleate reaction has finished, the contents of the precursor flask are pulled into a syringe for slow injection into the reaction flask. The injection rate is set to 0.2 mL/min and the injection volume depends on the desired NC size. Following the injection the reaction flask is allowed to stay at 290°C for 20 min before being cooled to room temperature. NC cores are washed by 5 cycles of flocculating NCs with ethanol, centrifuging at 7500 RPM, and redispersing in hexane. Overall NC size and size polydispersity were measured by small-angle x-ray scattering (SAXS) and verified by scanning transmission electron microscopy (STEM) image analysis (Figure S4-6). Overall dopant incorporation was quantified by elemental analysis using inductively coupled plasma-atomic emission spectroscopy (ICP-AES).

### Small-angle X-ray scattering measurements (SAXS)

SAXS measurements were performed in transmission configuration on a SAXSLAB Ganesha instrument using Cu K $\alpha$  radiation. The sample-detector distance was 1 m and 0.475 m for the NC doping series and NC size series, respectively. ITO NCs were dispersed in a 1:10 volume ratio of TCE:hexane and enclosed in glass capillaries (Charles-Supper Company, Boron Rich, 1.5 mm diameter, 0.01 mm wall thickness) sealed with epoxy. A capillary containing neat 1:10 volume ratio of TCE:hexane was used for background subtraction. Scattering patterns were calibrated using a silver behenate standard<sup>3</sup> and were converted into 1D data by circular averaging using the Igor Pro-based Nika software for two-dimensional data reduction.<sup>4</sup> The Irena tool suite for modeling and analysis in Igor Pro was used for background subtraction<sup>5</sup> and for fitting the NC form factor following a procedure described in a previous publication.<sup>6</sup> SAXS fit results are summarized in Table S1 & S2.

### Scanning transmission electron microscopy (STEM) measurements

STEM images were taken with a Hitachi S-5500. Samples for STEM measurements were drop cast on copper TEM grids with carbon supports (400 mesh, Ted Pella).

#### Spectroscopy measurements

Stock NC dispersions for optical measurements were prepared in a solution of 1.8 mM oleic acid in tetrachloroethylene (TCE). Dilute dispersions in 1.8 mM oleic acid in TCE were prepared from stock solutions immediately before optical measurement and dilution factors were calculated using mass fractions of stock to total solution for each sample. Optical measurements were taken on dilute dispersions in a 0.5 mm pathlength liquid cell. Infrared ( $650\text{-}4000\text{ cm}^{-1}$ ) and UV-visible-near infrared ( $3031\text{-}37000\text{ cm}^{-1}$ ) extinction were measured using a Bruker Vertex 70 FTIR spectrophotometer and Agilent Cary series UV-vis-NIR spectrophotometer, respectively. All spectra were taken in transmission mode and are reported as extinction. Spectra were backgrounded to a clean solution of 1.8 mM oleic acid in tetrachloroethylene (TCE) before each dilution series. The liquid cell was washed through with 1.8 mM oleic acid in TCE after each dilution series followed by the collection of an after spectrum to confirm the lack of NC deposition. All series reported in this work showed no evidence of deposition on the windows of the cell. NC volume fraction was determined using ICP-AES measurements of stock solutions. Fits to optical extinction spectra were conducted using a MATLAB code (SI Text 2).

#### Inductively coupled plasma-atomic emission spectroscopy (ICP-AES) measurements

The overall tin dopant concentration and volume fraction of ITO NCs were characterized by ICP-AES on a Varian 720-ES ICP Optical Emission Spectrometer after digesting the NCs with aqua regia. The volume fraction of ITO was calculated from the concentration of In and Sn in the analyte using an assumed stoichiometry of  $(\text{In}+\text{Sn})_2\text{O}_3$  and density of 7140 mg/mL.

#### Author Contributions

C.M.S. wrote the HEDA model, synthesized, characterized (SEM and ICP-AES), and measured and fit optical extinction of ITO NCs. A.A. assisted in conceptualizing and writing the HEDA model. S.L.G. developed colloidal NC optical measurement techniques. C.A.S.C. conducted and analyzed SAXS measurements. R.W.J. assisted in experimental design and contributed intellectually. D.J.M. provided overall guidance. C.M.S. and D.J.M. wrote the manuscript with critical input from all the authors.

#### Author Information

Corresponding Author

E-mail: [milliron@che.utexas.edu](mailto:milliron@che.utexas.edu)

Notes:

The authors declare no competing financial interest.

#### Associated Content

Details of validation of mesh size, single NC optical extinction simulations, validation of near surface dopant activation, NC STEM images, SAXS analysis, Tauc plots, Extinction coefficients in various units, NC ensemble optical fits and variables, comparison of average NC and

ensemble optical extinction, Mie theory extinction coefficient analytical solution, checking variable correlations, and MATLAB code.

### Acknowledgements

This research was supported by the National Science Foundation (NSF), including NASCENT, an NSF ERC (EEC-1160494, C.M.S.), CHE-1609656 (A.A.), the University of Texas at Austin MRSEC (DMR-1720595, C.A.S.C.), a Graduate Research Fellowship under Award Number (DGE-1610403, S.L.G.), and the Welch Foundation (F-1848, R.W.J.). This work was performed at UT Austin and utilized the SAXS instrument acquired under an NSF MRI grant (CBET-1624659) and in part at the Molecular Foundry, Lawrence Berkeley National Laboratory, which is supported by the Office of Science, Office of Basic Energy Sciences, of the U.S. Department of Energy (DOE) under Contract No. DE-AC02-05CH11231.

### References

1. Garcia, G. *et al.* Dynamically Modulating the Surface Plasmon Resonance of Doped Semiconductor Nanocrystals. *Nano Lett.* **11**, 4415–4420 (2011).
2. Wang, Y., Runnerstrom, E. L. & Milliron, D. J. Switchable Materials for Smart Windows. *Annu. Rev. Chem. Biomol. Eng.* **7**, 283–304 (2016).
3. Llordés, A., Garcia, G., Gazquez, J. & Milliron, D. J. Tunable near-infrared and visible-light transmittance in nanocrystal-in-glass composites. *Nature* **500**, 323–326 (2013).
4. Anker, J. N. *et al.* Biosensing with plasmonic nanosensors. *Nature Materials* **7**, 442–453 (2008).
5. Mayer, K. M. & Hafner, J. H. Localized Surface Plasmon Resonance Sensors. *Chem. Rev.* **111**, 3828–3857 (2011).
6. Neubrech, F., Huck, C., Weber, K., Pucci, A. & Giessen, H. Surface-Enhanced Infrared Spectroscopy Using Resonant Nanoantennas. *Chem. Rev.* **117**, 5110–5145 (2017).
7. Willets, K. A. & Van Duyne, R. P. Localized Surface Plasmon Resonance Spectroscopy and Sensing. *Annu. Rev. Phys. Chem.* **58**, 267–297 (2007).
8. Stiles, P. L., Dieringer, J. A., Shah, N. C. & Van Duyne, R. P. Surface-Enhanced Raman Spectroscopy. *Annu. Rev. Anal. Chem.* **1**, 601–626 (2008).

9. Kneipp, K. *et al.* Single Molecule Detection Using Surface-Enhanced Raman Scattering (SERS). *Phys. Rev. Lett.* **78**, 1667–1670 (1997).
10. Harris, N., Ford, M. J. & Cortie, M. B. Optimization of Plasmonic Heating by Gold Nanospheres and Nanoshells. *J. Phys. Chem. B* **110**, 10701–10707 (2006).
11. Herzog, J. B., Knight, M. W. & Natelson, D. Thermoplasmonics: Quantifying Plasmonic Heating in Single Nanowires. *Nano Lett.* **14**, 499–503 (2014).
12. Donner, J. S. *et al.* Imaging of Plasmonic Heating in a Living Organism. *ACS Nano* **7**, 8666–8672 (2013).
13. Cole, J. R., Mirin, N. A., Knight, M. W., Goodrich, G. P. & Halas, N. J. Photothermal Efficiencies of Nanoshells and Nanorods for Clinical Therapeutic Applications. *J. Phys. Chem. C* **113**, 12090–12094 (2009).
14. Hirsch, L. R. *et al.* Nanoshell-mediated near-infrared thermal therapy of tumors under magnetic resonance guidance. *Proc. Natl. Acad. Sci.* **100**, 13549–13554 (2003).
15. Gobin, A. M. *et al.* Near-Infrared Resonant Nanoshells for Combined Optical Imaging and Photothermal Cancer Therapy. *Nano Lett.* **7**, 1929–1934 (2007).
16. Schimpf, A. M., Lounis, S. D., Runnerstrom, E. L., Milliron, D. J. & Gamelin, D. R. Redox Chemistries and Plasmon Energies of Photodoped  $\text{In}_2\text{O}_3$  and Sn-Doped  $\text{In}_2\text{O}_3$  (ITO) Nanocrystals. *J. Am. Chem. Soc.* **137**, 518–524 (2015).
17. Schimpf, A. M., Ochsenbein, S. T., Buonsanti, R., Milliron, D. J. & Gamelin, D. R. Comparison of extra electrons in colloidal n-type  $\text{Al}^{3+}$ -doped and photochemically reduced ZnO nanocrystals. *Chem. Commun.* **48**, 9352–9354 (2012).
18. Agrawal, A. *et al.* Localized Surface Plasmon Resonance in Semiconductor Nanocrystals. *Chem. Rev.* **118**, 3121–3207 (2018).
19. Jain, P. K., Lee, K. S., El-Sayed, I. H. & El-Sayed, M. A. Calculated Absorption and Scattering Properties of Gold Nanoparticles of Different Size, Shape, and Composition:

- Applications in Biological Imaging and Biomedicine. *J. Phys. Chem. B* **110**, 7238–7248 (2006).
20. Lee, K.-S. & El-Sayed, M. A. Gold and Silver Nanoparticles in Sensing and Imaging: Sensitivity of Plasmon Response to Size, Shape, and Metal Composition. *J. Phys. Chem. B* **110**, 19220–19225 (2006).
  21. L. Nehl, C. & H. Hafner, J. Shape-dependent plasmon resonances of gold nanoparticles. *J. Mater. Chem.* **18**, 2415–2419 (2008).
  22. Chen, H., Kou, X., Yang, Z., Ni, W. & Wang, J. Shape- and Size-Dependent Refractive Index Sensitivity of Gold Nanoparticles. *Langmuir* **24**, 5233–5237 (2008).
  23. Aksu, S. *et al.* High-Throughput Nanofabrication of Infrared Plasmonic Nanoantenna Arrays for Vibrational Nanospectroscopy. *Nano Lett.* **10**, 2511–2518 (2010).
  24. Adato, R. & Altug, H. *In-situ* ultra-sensitive infrared absorption spectroscopy of biomolecule interactions in real time with plasmonic nanoantennas. *Nat. Commun.* **4**, 2154 (2013).
  25. Neuman, T. *et al.* Importance of Plasmonic Scattering for an Optimal Enhancement of Vibrational Absorption in SEIRA with Linear Metallic Antennas. *J. Phys. Chem. C* **119**, 26652–26662 (2015).
  26. Abb, M., Wang, Y., Papasimakis, N., de Groot, C. H. & Muskens, O. L. Surface-Enhanced Infrared Spectroscopy Using Metal Oxide Plasmonic Antenna Arrays. *Nano Lett.* **14**, 346–352 (2014).
  27. Bukasov, R. & Shumaker-Parry, J. S. Silver Nanocrescents with Infrared Plasmonic Properties As Tunable Substrates for Surface Enhanced Infrared Absorption Spectroscopy. *Anal. Chem.* **81**, 4531–4535 (2009).
  28. Adato, R. *et al.* Ultra-sensitive vibrational spectroscopy of protein monolayers with plasmonic nanoantenna arrays. *Proc. Natl. Acad. Sci.* **106**, 19227–19232 (2009).

29. Kundu, J., Le, F., Nordlander, P. & Halas, N. J. Surface enhanced infrared absorption (SEIRA) spectroscopy on nanoshell aggregate substrates. *Chem. Phys. Lett.* **452**, 115–119 (2008).
30. Huang, X., El-Sayed, I. H., Qian, W. & El-Sayed, M. A. Cancer Cell Imaging and Photothermal Therapy in the Near-Infrared Region by Using Gold Nanorods. *J. Am. Chem. Soc.* **128**, 2115–2120 (2006).
31. El-Sayed, I. H. Nanotechnology in Head and Neck Cancer: The Race Is On. *Curr. Oncol. Rep.* **12**, 121–128 (2010).
32. Bohren, C. & Huffman, D. *Absorption and Scattering of Light by Small Particles*. (Wiley, 1983).
33. Wokaun, A., Gordon, J. P. & Liao, P. F. Radiation Damping in Surface-Enhanced Raman Scattering. *Phys. Rev. Lett.* **48**, 957–960 (1982).
34. Link, S. & El-Sayed, M. A. Spectral Properties and Relaxation Dynamics of Surface Plasmon Electronic Oscillations in Gold and Silver Nanodots and Nanorods. *J. Phys. Chem. B* **103**, 8410–8426 (1999).
35. Zandi, O. *et al.* Impacts of surface depletion on the plasmonic properties of doped semiconductor nanocrystals. *Nat. Mater.* **17**, 710 (2018).
36. Agrawal, A. *et al.* Rationalizing the Impact of Surface Depletion on Electrochemical Modulation of Plasmon Resonance Absorption in Metal Oxide Nanocrystals. *ACS Photonics* **5**, 2044–2050 (2018).
37. Staller, C. M. *et al.* Tuning Nanocrystal Surface Depletion by Controlling Dopant Distribution as a Route Toward Enhanced Film Conductivity. *Nano Lett.* **18**, 2870–2878 (2018).
38. Jansons, A. W. & Hutchison, J. E. Continuous Growth of Metal Oxide Nanocrystals: Enhanced Control of Nanocrystal Size and Radial Dopant Distribution. *ACS Nano* **10**, 6942–6951 (2016).



39. Johns, R. W. *et al.* Direct observation of narrow mid-infrared plasmon linewidths of single metal oxide nanocrystals. *Nat. Commun.* **7**, 11583 (2016).
40. Frank, G. & Köstlin, H. Electrical properties and defect model of tin-doped indium oxide layers. *Appl. Phys. A* **27**, 197–206 (1982).
41. Lounis, S. D., Runnerstrom, E. L., Llordés, A. & Milliron, D. J. Defect Chemistry and Plasmon Physics of Colloidal Metal Oxide Nanocrystals. *J. Phys. Chem. Lett.* **5**, 1564–1574 (2014).
42. Rance, G. A., Marsh, D. H. & Khlobystov, A. N. Extinction coefficient analysis of small alkanethiolate-stabilised gold nanoparticles. *Chem. Phys. Lett.* **460**, 230–236 (2008).
43. Ding, X. *et al.* Seeded Growth of  $\text{Cu}_{2-x}\text{Se}$  Nanocrystals and Their Size-Dependent Phototherapeutic Effect. *ACS Appl. Nano Mater.* **1**, 3303–3311 (2018).
44. Dai, Q. *et al.* Size-Dependent Composition and Molar Extinction Coefficient of PbSe Semiconductor Nanocrystals. *ACS Nano* **3**, 1518–1524 (2009).
45. Kreibig, U. & Frangstein, C. v. The limitation of electron mean free path in small silver particles. *Z. Für Phys.* **224**, 307–323 (1969).
46. Moroz, A. Electron Mean Free Path in a Spherical Shell Geometry. *J. Phys. Chem. C* **112**, 10641–10652 (2008).
47. Tahar, R. B. H., Ban, T., Ohya, Y. & Takahashi, Y. Tin doped indium oxide thin films: Electrical properties. *J. Appl. Phys.* **83**, 2631–2645 (1998).
48. Lounis, S. D., Runnerstrom, E. L., Bergerud, A., Nordlund, D. & Milliron, D. J. Influence of Dopant Distribution on the Plasmonic Properties of Indium Tin Oxide Nanocrystals. *J. Am. Chem. Soc.* **136**, 7110–7116 (2014).
49. Agrawal, A., Johns, R. W. & Milliron, D. J. Control of Localized Surface Plasmon Resonances in Metal Oxide Nanocrystals. *Annu. Rev. Mater. Res.* **47**, null (2017).

50. W. Johns, R. *et al.* Charge carrier concentration dependence of ultrafast plasmonic relaxation in conducting metal oxide nanocrystals. *J. Mater. Chem. C* (2017).

### Methods References

1. Jansons, A. W. & Hutchison, J. E. Continuous Growth of Metal Oxide Nanocrystals: Enhanced Control of Nanocrystal Size and Radial Dopant Distribution. *ACS Nano* **10**, 6942–6951 (2016).
2. Crockett, B. M., Jansons, A. W., Koskela, K. M., Johnson, D. W. & Hutchison, J. E. Radial Dopant Placement for Tuning Plasmonic Properties in Metal Oxide Nanocrystals. *ACS Nano* **11**, 7719–7728 (2017).
3. Hexemer, A. *et al.* A SAXS/WAXS/GISAXS Beamline with Multilayer Monochromator. *J. Phys. Conf. Ser.* **247**, 012007 (2010).
4. Ilavsky, J. Nika: software for two-dimensional data reduction. *J. Appl. Crystallogr.* **45**, 324–328 (2012).
5. Ilavsky, J. & Jemian, P. R. Irena: tool suite for modeling and analysis of small-angle scattering. *J. Appl. Crystallogr.* **42**, 347–353 (2009).
6. Singh, A. *et al.* Linking Semiconductor Nanocrystals into Gel Networks through All-Inorganic Bridges. *Angew. Chem. Int. Ed.* **54**, 14840–14844 (2015).

## Supporting Information

### Quantitative Analysis of Optical Extinction Properties of Semiconductor Nanocrystals

Corey M. Staller<sup>†</sup>, Ankit Agrawal<sup>†</sup>, Stephen L. Gibbs<sup>†</sup>, Camila A. Saez Cabezas<sup>†</sup>, Robert W. Johns<sup>||,†</sup>, Delia J. Milliron<sup>\*,†</sup>

<sup>†</sup> McKetta Department of Chemical Engineering, University of Texas at Austin, Austin, Texas, 78712-1589, United States

<sup>||</sup> Department of Chemistry, University of California, Berkeley, Berkeley, California 94720, USA

Corresponding Author

E-mail: [milliron@che.utexas.edu](mailto:milliron@che.utexas.edu)

Telephone: (512)232-5702

KEYWORDS: Nanocrystal, Tin-doped Indium Oxide, Extinction Coefficient, Surface Scattering, Polydispersity, Depletion

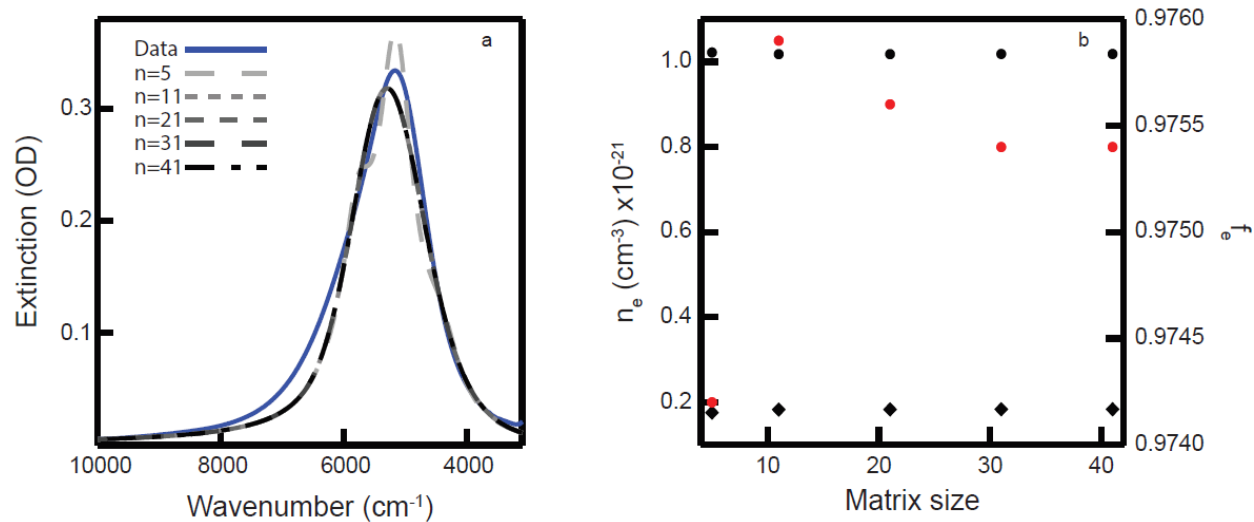


**Figure S1. Verification of mesh size.** HEDA model fits to 20 nm 6 at% ITO NCs of varying probability matrix dimensions,  $n$ , (a) and resulting variables (b). Fitted variables become constant at  $n=31$ . Results presented in the paper represent  $n=41$  to ensure stabilization of fit parameters.

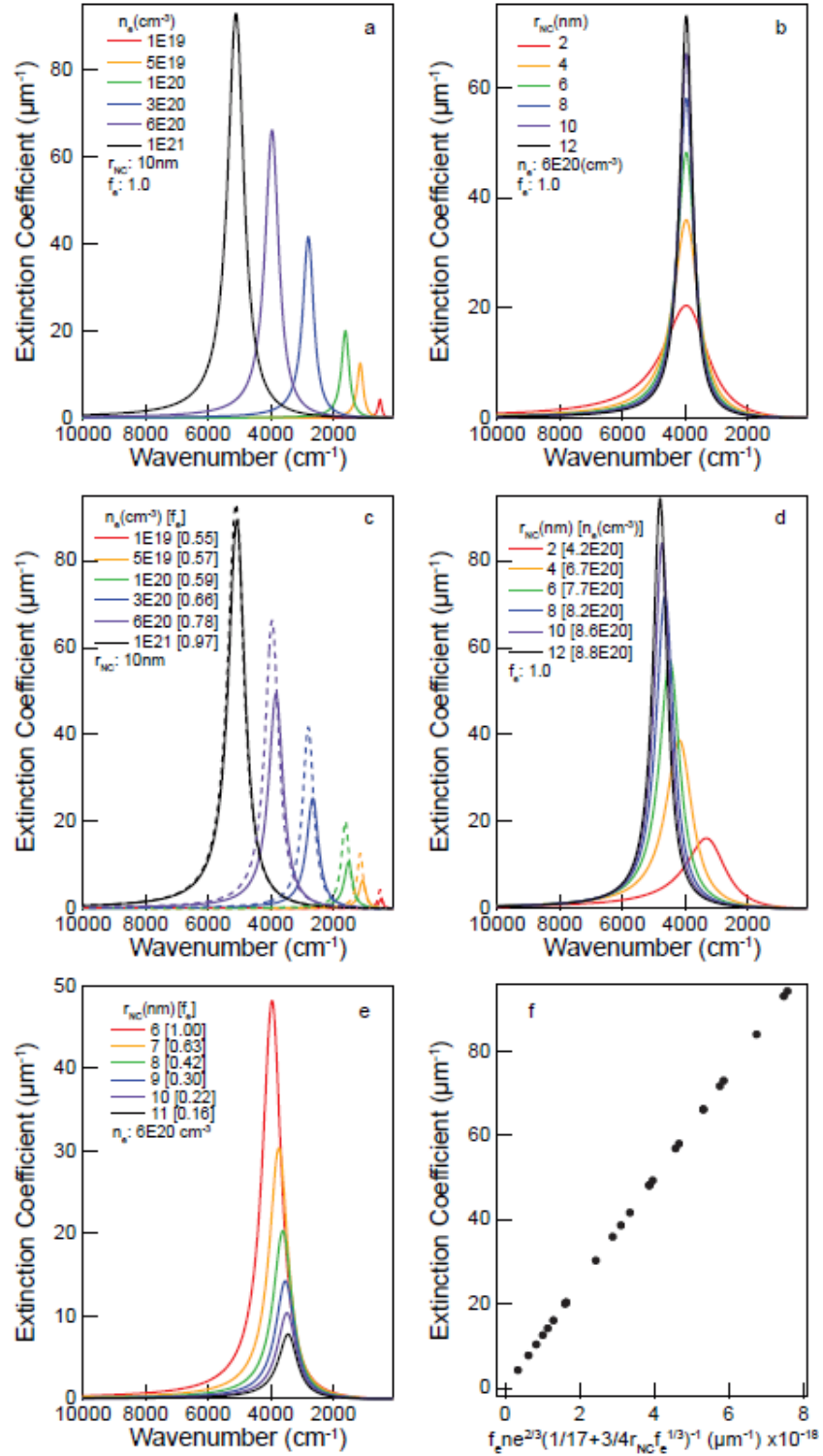


**Figure S2. Simulated LSPR spectra** with varying electron concentration (a), NC radius (b), electron concentration with a calculated depletion using a linear fit to Figure 5d (c), radius with a calculated electron concentration using a 0.5 nm surface deactivation layer (d), and depletion (e), and LSPR peak extinction coefficient v.  $f_e \frac{\omega_p^2}{\Gamma}$ .

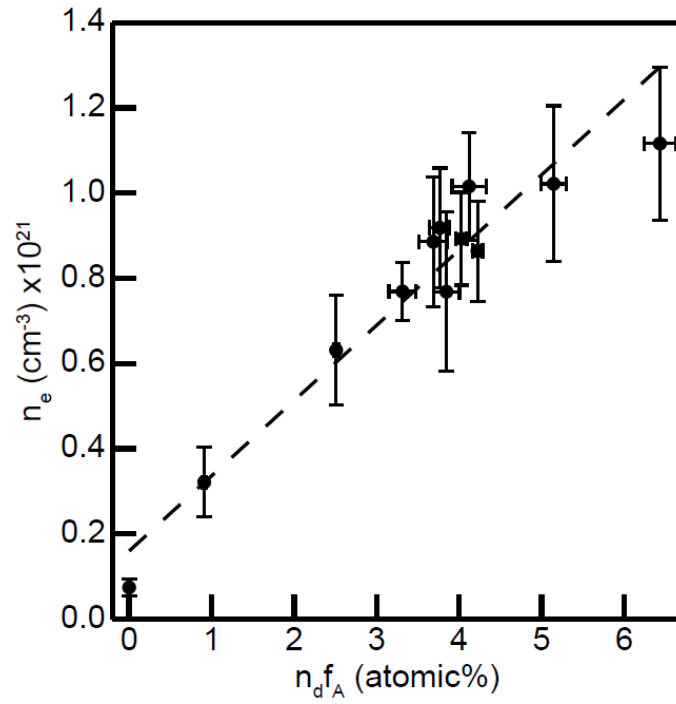


**Figure S3. Dopant activation v. non-surface dopant concentration.** HEDA model fits to samples measured show electron concentration increases with  $n_d f_A$  as predicted by decreased near-surface dopant activation.

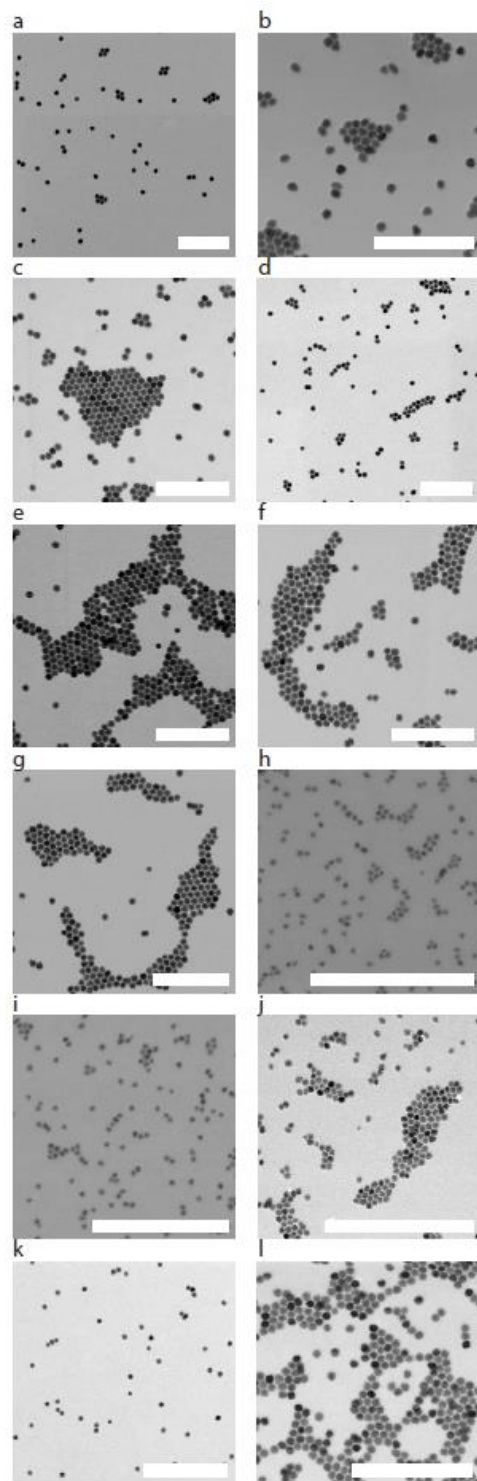


**Figure S4. STEM images** of 20 nm 0 at% (a), 1 at% (b), 3 at% (c), 4.5 at% (d), 5 at% (e), 6 at% (f), and 7.5 at% (g) ITO NCs and 6 nm (h), 8 nm (i), 11 nm (j), 12 nm (k), and 14 nm (l) 5 at% ITO NCs. Scale bars represent 200 nm.

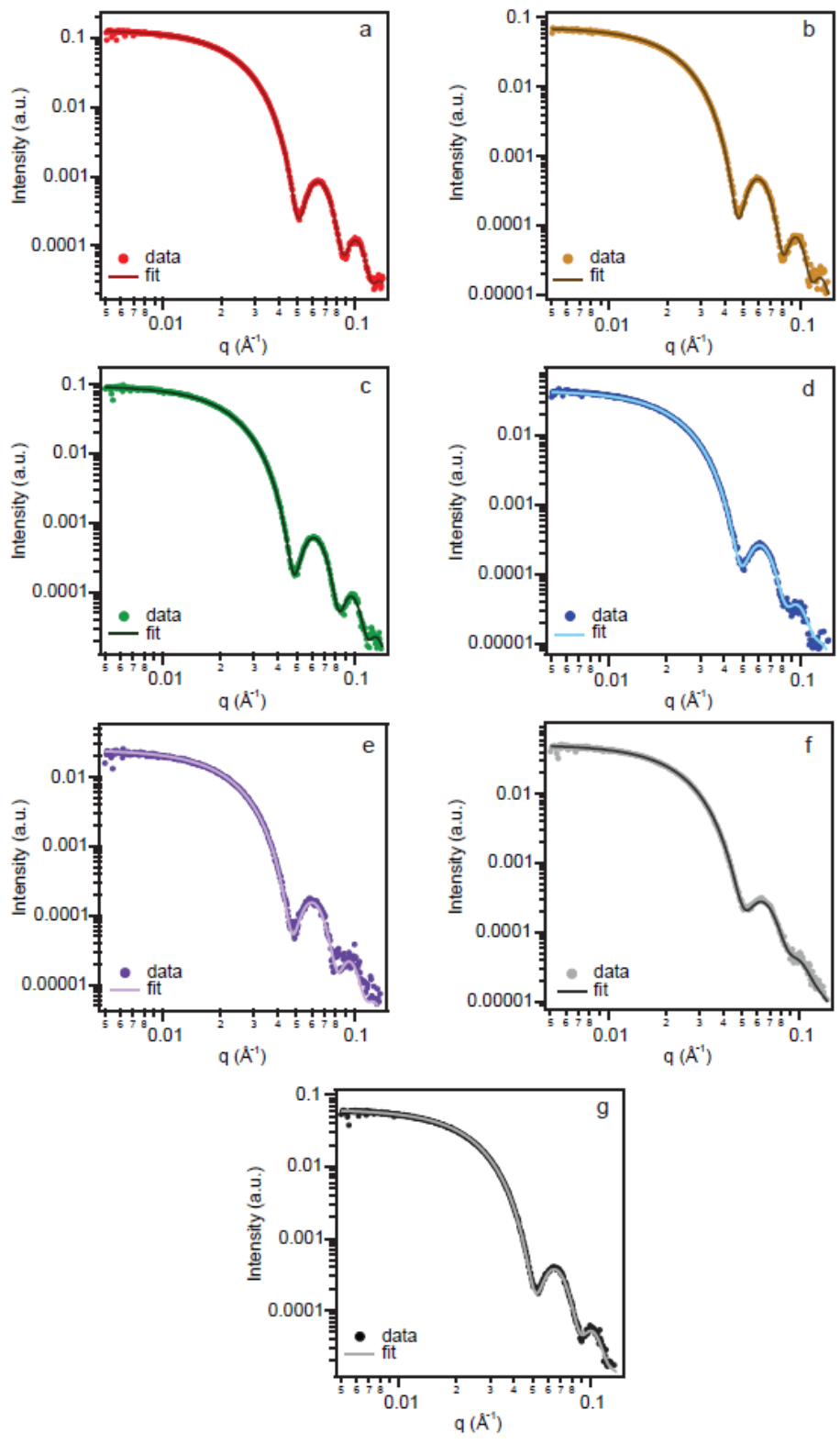


**Figure S5.** SAXS of 20 nm 0 at% (a), 1 at% (b), 3 at% (c), 4.5 at% (d), 5 at% (e), 6.5 at% (f), and 8 at% (g) ITO NCs ITO NCs.



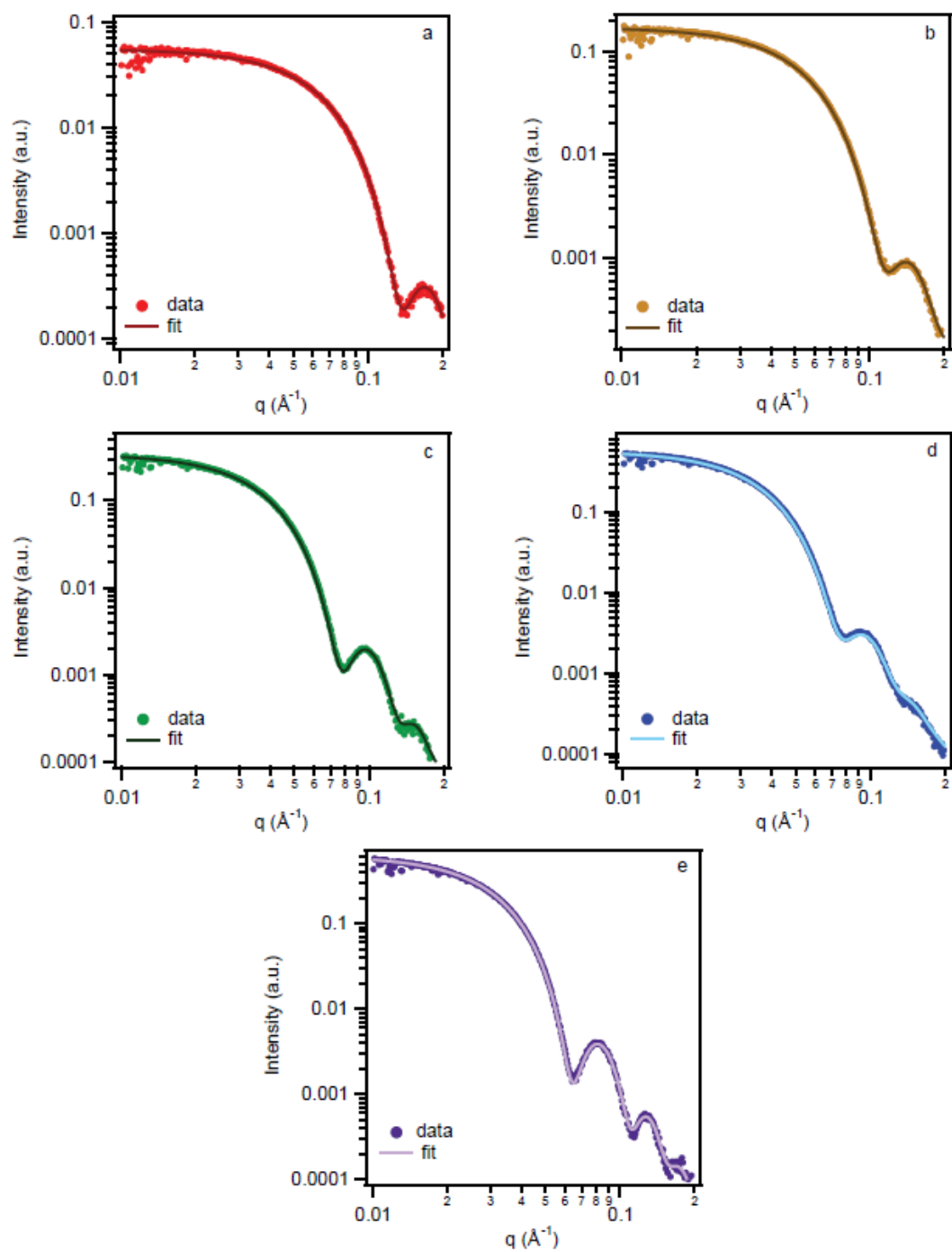


**Figure S6.** SAXS of 6 nm (a), 8 nm (b), 11 nm (c), 12 nm (d), and 14 nm (e) 5 at% ITO NCs.

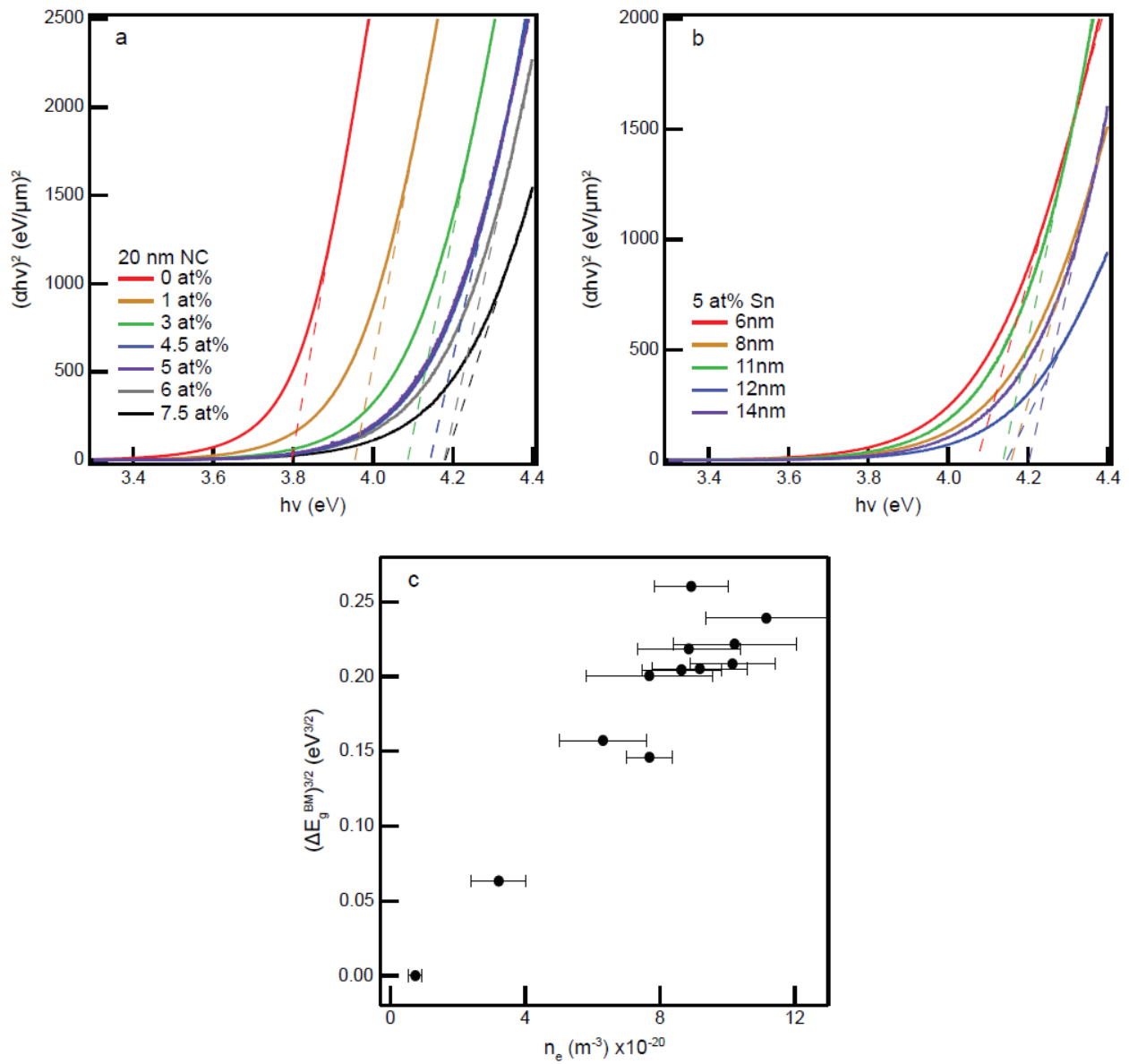


**Figure S7.** Tauc plots of ITO NCs showing optical bandgap widening with increasing dopant concentration (a) and NC radius (b).

**Table S1. Extinction coefficient of NCs and NPs in a variety of units.**

	atomic% Sn	$r_{NC}$ (nm)	Extinction coefficient $\epsilon$ ( $\mu\text{m}^{-1}$ )	Extinction cross section		Molar extinction coefficient $M^{-1}\text{cm}^{-1}$	Extinction coefficient $\text{mL mg}^{-1}\text{cm}^{-1}$
				$\mu\text{m}^2$	$\text{m}^2$		
ITO NCs	0	8.9	4.51	1.3E-05	1.3E-17	3.49E+07	2.74
	1.07	9.6	15.14	5.5E-05	5.5E-17	1.45E+08	9.21
	2.96	9.3	29.12	9.8E-05	9.8E-17	2.57E+08	17.71
	4.45	9.2	51.02	1.7E-04	1.7E-16	4.39E+08	31.03
	4.97	9.5	51.91	1.8E-04	1.8E-16	4.82E+08	31.57
	6.13	8.8	51.94	1.5E-04	1.5E-16	3.88E+08	31.59
	7.68	8.7	56.55	1.6E-04	1.6E-16	4.10E+08	34.40
	5.42	3.3	13.58	2.1E-06	2.1E-18	5.38E+06	8.26
	5.54	3.9	24.37	6.2E-06	6.2E-18	1.63E+07	14.82
	5.03	5.8	33.36	2.8E-05	2.8E-17	7.26E+07	20.29
	5.36	6.0	47.45	4.2E-05	4.2E-17	1.10E+08	28.86
	5.03	7.0	47.14	6.8E-05	6.8E-17	1.78E+08	28.68
	4.97	9.5	51.91	1.8E-04	1.8E-16	4.82E+08	31.57
Au spherical NPs	-	10.0	73.70	3.1E-04	3.1E-16	8.07E+08	16.58
Cu <sub>2-x</sub> Se NCs	-	17.5	23.50	5.3E-04	5.3E-16	1.38E+09	15.01
PbSe QDs	-	2.75	12.70	1.1E-06	1.1E-18	2.89E+06	6.81

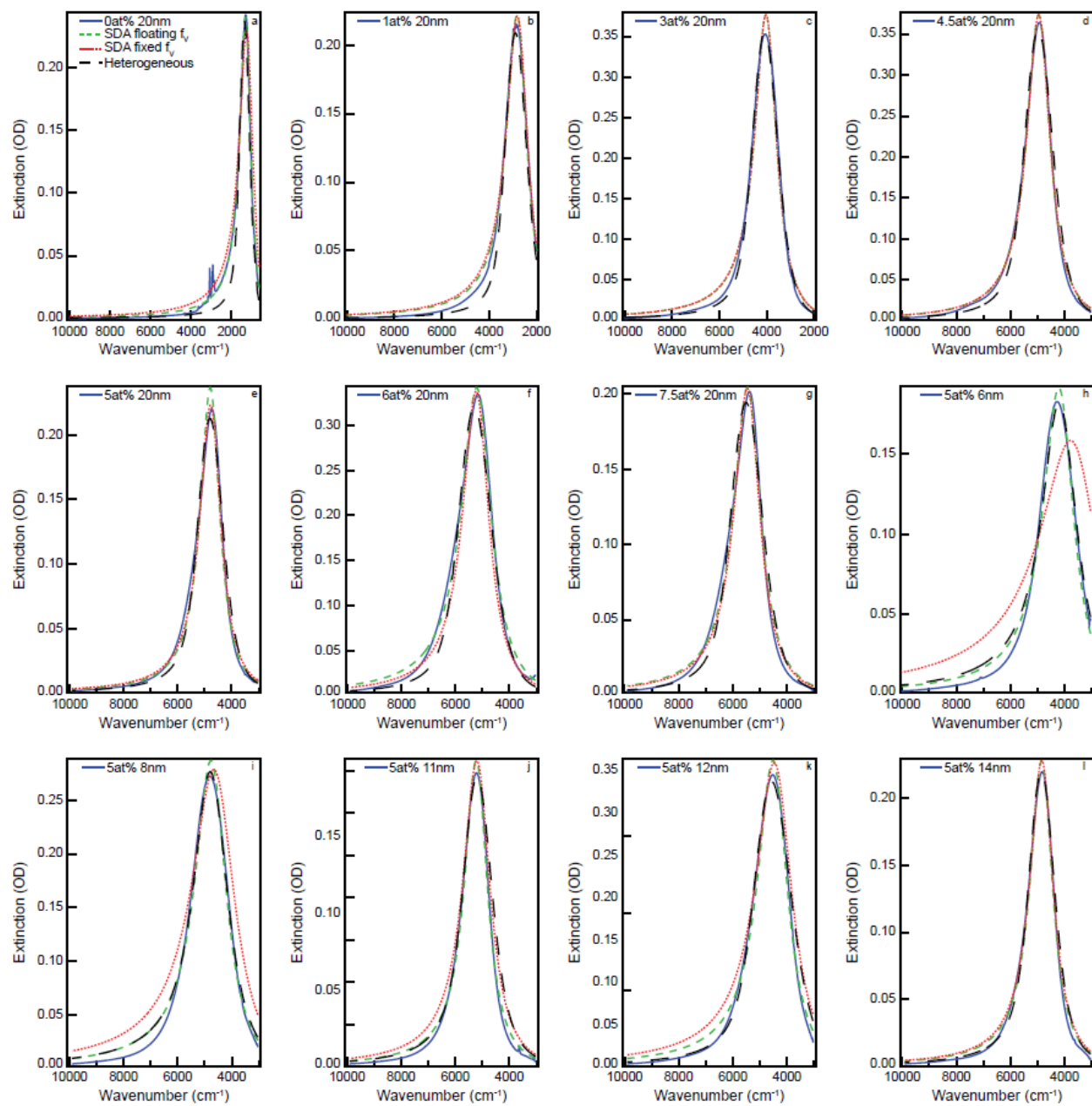


**Figure S8. Optical extinction fits** with simple Drude approximation (SDA) with a floating NC loading, SDA with measured NC loading, and Heterogeneous Ensemble Drude Approximation (HEDA) model for 20 nm 0 at% (a), 1 at% (b), 3 at% (c), 4.5 at% (d), 5 at% (e), 6.5 at% (f), and 8 at% (g) ITO NCs and 8 nm (h), 9 nm (i), 13 nm (j), 14 nm (k), and 16 nm (l) 5 at% ITO NCs.

**Table S2. Dopant concentration series optical extinction fit parameters.**

Sample Details	At% Sn	0	1.07	2.97	4.45	6.13	7.68
	$\mu_r$ (nm)	8.91	9.56	9.31	9.23	8.80	8.72
	$\sigma_r$ (nm)	0.65	0.66	0.68	0.88	1.05	0.792
	$f_v$ from ICP	2.44E-04	6.44E-05	5.43E-05	3.30E-05	2.98E-05	3.27E-05
SDA w/ Floating $f_v$	$f_v$	1.90E-04	6.07E-05	5.37E-05	3.28E-05	3.48E-05	3.43E-05
	$w_p$ (cm <sup>-1</sup> )	3831	8234	11777	14469	15236	15950
	Damping (cm <sup>-1</sup> )	667	1065	1138	1060	1360	1229
	$n_e$ (cm <sup>-3</sup> )	6.6E19	3.0E20	6.2E20	9.3E20	1.0E21	1.1E21
SDA w/ Fixed $f_v$	$w_p$ (cm <sup>-1</sup> )	3691	8199	11771	14468	15294	15963
	Damping (cm <sup>-1</sup> )	835	1126	1149	1064	1189	1178
	$n_e$ (cm <sup>-3</sup> )	6.1E19	3.0E20	6.2E20	9.3E20	1.0E21	1.1E21
HEDA	$\mu_{ne}$ (cm <sup>-3</sup> )	7.4E19	3.2E20	6.2E20	9.2E20	1.0E21	1.1E21
	$\sigma_{ne}$ (cm <sup>-3</sup> )	2.1E19	8.4E19	1.3E20	1.4E20	1.8E20	1.8E20
	$f_e$	0.51	0.69	0.87	0.95	0.97	0.98
Calculated HEDA Damping (cm <sup>-1</sup> )	398	573	694	781	830	860	

$\mu_r$  and  $\sigma_r$  are the mean NC radius and its standard deviation,  $f_v$  is the NC volume fraction in solution,  $w_p$  is the plasma frequency,  $n_e$  is the electron concentration,  $\mu_{ne}$  and  $\sigma_{ne}$  are the mean electron concentration and its standard deviation, and  $f_e$  is the fraction of electron accessible volume.

**Table S3. NC size series optical extinction fit parameters.**

Sample Details	At% Sn	5.42	5.54	5.03	5.36	5.03	4.97
	$\mu_r$ (nm)	3.31	3.94	5.83	5.96	7.01	9.46
	$\sigma_r$ (nm)	0.36	0.48	0.76	0.58	0.55	0.76
	$f_v$ from ICP	6.06E-05	5.05E-05	3.30E-05	3.35E-05	2.12E-05	7.72E-06
SDA w/ Floating $f_v$	$f_v$	3.07E-05	3.65E-05	2.70E-05	2.80E-05	2.02E-05	7.47E-06
	$w_p$ (cm <sup>-1</sup> )	12305	13932	13204	15261	14159	13995
	Damping (cm <sup>-1</sup> )	1398	1419	1359	1037	1022	890
	$n_e$ (cm <sup>-3</sup> )	6.8E20	8.7E20	7.8E20	1.0E21	9.0E20	8.7E20
SDA w/ Fixed $f_v$	$w_p$ (cm <sup>-1</sup> )	11035	13622	13055	15196	14143	13965
	Damping (cm <sup>-1</sup> )	2683	1936	1632	1232	1072	970
	$n_e$ (cm <sup>-3</sup> )	5.4E20	8.3E20	7.6E20	1.0E21	8.9E20	8.7E20
HEDA	$\mu_{ne}$ (cm <sup>-3</sup> )	7.7E20	8.9E20	7.7E20	1.0E21	8.9E20	8.6E20
	$\sigma_{ne}$ (cm <sup>-3</sup> )	6.8E19	1.5E20	1.9E20	1.3E20	1.1E20	1.2E20
	$f_e$	0.47	0.72	0.79	0.93	0.93	0.95
Calculated HEDA Damping (cm <sup>-1</sup> )	1947	1560	1063	1104	938	753	

$\mu_r$  and  $\sigma_r$  are the mean NC radius and its standard deviation,  $f_v$  is the NC volume fraction in solution,  $w_p$  is the plasma frequency,  $n_e$  is the electron concentration,  $\mu_{ne}$  and  $\sigma_{ne}$  are the mean electron concentration and its standard deviation, and  $f_e$  is the fraction of electron accessible volume.

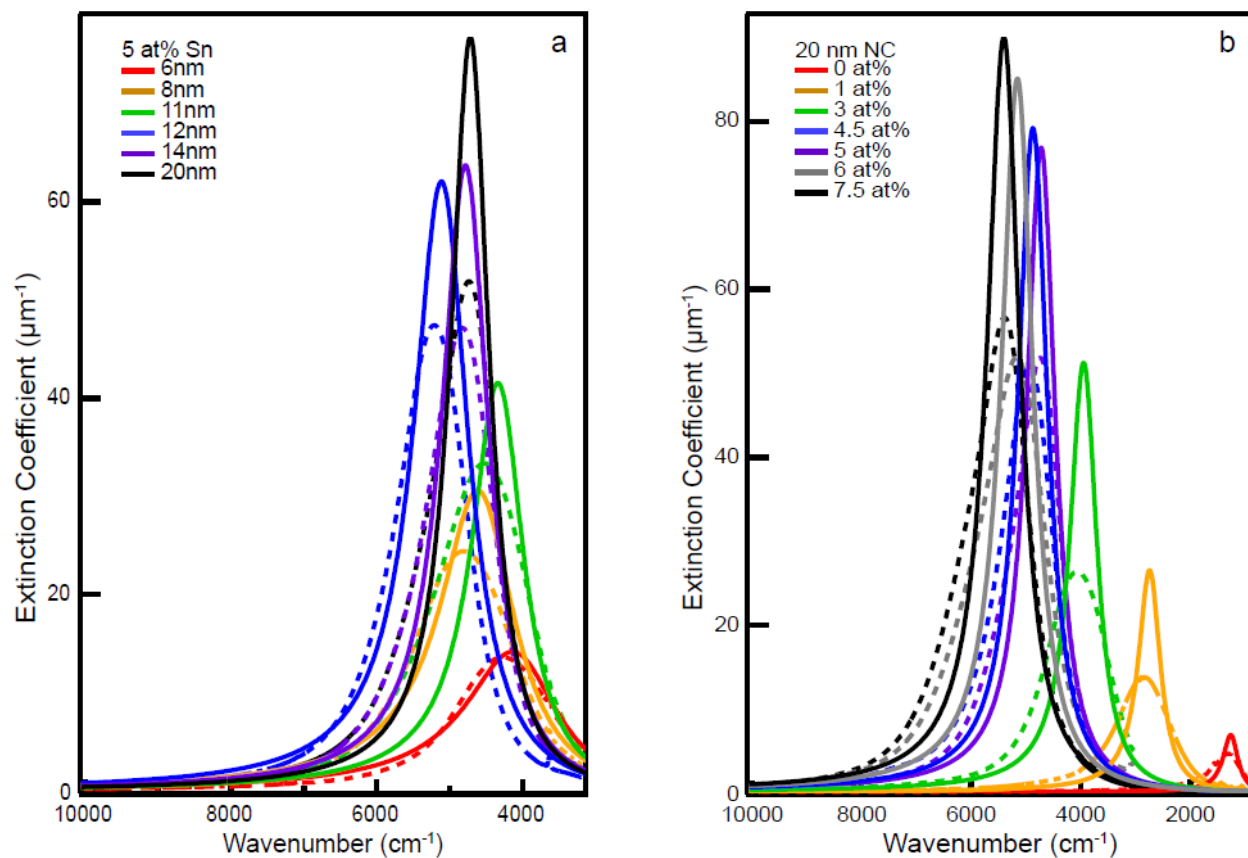


**Figure S9. Average NC LSPR absorption spectra compared to ensemble absorption.** Average NC absorption coefficient (solid) is higher and shows a narrower lineshape than ensemble absorption coefficient (dashed).

## SI Text 1. Mie Theory LSPR Peak Extinction Coefficient

Starting from the Drude-Lorentz dielectric function,

$$\epsilon_{NC}(\omega) = \epsilon_{\infty} - \frac{\omega_p^2}{\omega^2 + i\omega\Gamma} \quad \text{S1}$$

The NC dielectric function can be described as a summation of the real and imaginary parts of the dielectric function

$$\epsilon_{NC}(\omega) = \epsilon_1(\omega) + i\epsilon_2(\omega) \quad \text{S2}$$

Where

$$\epsilon_1(\omega) = \epsilon_{\infty} - \frac{\omega_p^2}{\omega^2 + \Gamma^2} \quad \text{S3a}$$

and

$$\epsilon_2(\omega) = \frac{\omega_p^2\Gamma}{\omega(\omega^2 + \Gamma^2)} \quad \text{S3b}$$

Plugging the dielectric function into the Mie Theory absorption coefficient

$$\epsilon_{NC} = \frac{\sigma}{V_{NC}} = 6\pi\omega\sqrt{\epsilon_m} \text{Imag} \left\{ \frac{\epsilon_{NC}(\omega) - \epsilon_m}{\epsilon_{NC}(\omega) + 2\epsilon_m} \right\} = 6\pi\omega\sqrt{\epsilon_m} \text{Imag} \left\{ \frac{\epsilon_1(\omega) + i\epsilon_2(\omega) - \epsilon_m}{\epsilon_1(\omega) + i\epsilon_2(\omega) + 2\epsilon_m} \right\} \quad \text{S4}$$

The LSPR condition is defined by

$$\epsilon_1(\omega) = -2\epsilon_m \quad \text{S5}$$

Plugging S5 in S4

$$\epsilon_{NC} = 6\pi\omega_{LSPR}\sqrt{\epsilon_m} \text{Imag} \left\{ \frac{i\epsilon_2 - 3\epsilon_m}{i\epsilon_2} \right\} \quad \text{S6}$$

S6 simplifies to

$$\epsilon_{NC} = 18\pi\omega_{LSPR}\sqrt{\epsilon_m} \frac{\epsilon_m}{\epsilon_2} \quad \text{S7}$$

The imaginary part of the dielectric is solved for as

$$\epsilon_1 = \epsilon_{\infty} - \frac{\omega_p^2}{\omega_{LSPR}^2 + \Gamma^2} = -2\epsilon_m \rightarrow \frac{\omega_p^2}{\omega_{LSPR}^2 + \Gamma^2} = \epsilon_{\infty} + 2\epsilon_m \quad \text{S8a}$$

$$\epsilon_2(\omega) = \frac{\omega_p^2\Gamma}{\omega_{LSPR}(\omega_{LSPR}^2 + \Gamma^2)} = \left( \frac{\Gamma}{\omega_{LSPR}} \right) \left( \frac{\omega_p^2}{\omega_{LSPR}^2 + \Gamma^2} \right) = \left( \frac{\Gamma}{\omega_{LSPR}} \right) (\epsilon_{\infty} + 2\epsilon_m) \quad \text{S8b}$$

Plugging S8b into S7

$$\epsilon_{NC} = 18\pi\epsilon_m^{\frac{3}{2}} \frac{\omega_{LSPR}^2}{\Gamma} \quad \text{S9}$$

The relationship between  $\omega_{LSPR}$  and  $\omega_p$  is found by

$$\epsilon_1 = \epsilon_\infty - \frac{\omega_p^2}{\omega_{LSPR}^2 + \Gamma^2} = -2\epsilon_m \rightarrow \omega_{LSPR}^2 = \frac{\omega_p^2}{\epsilon_\infty + 2\epsilon_m} - \Gamma^2 \quad \text{S10}$$

Finally, plugging S10 into S9

$$\epsilon_{NC} = 18\pi\epsilon_m^{\frac{3}{2}} \left( \frac{\omega_p^2}{\Gamma(\epsilon_\infty + 2\epsilon_m)} - \Gamma \right) \quad \text{S11}$$

It is clear from S11 that when  $\omega_p \gg \Gamma$ ,  $\epsilon_{NC} \propto \frac{\omega_p^2}{\Gamma} \propto n_e^{\frac{2}{3}} * \left( \frac{1}{17} + \frac{1}{\frac{4}{3}\Gamma_{NC}f_e^{\frac{1}{3}}} \right)^{-1}$



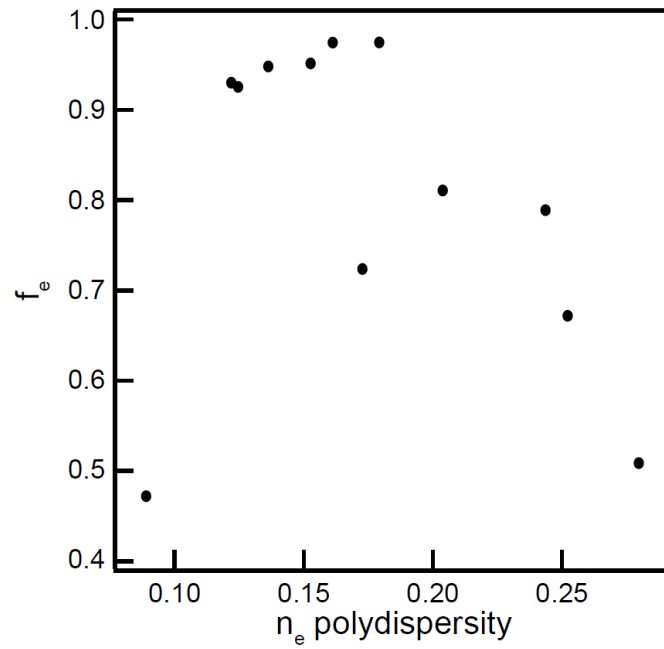


**Figure S10. Rationalizing optical parameters.** Plasmonic volume fraction (HEDA model fit  $f_e$ ), which contributes to average NC damping, and heterogeneous broadening (HEDA model fit electron concentration polydispersity,  $\sigma_{n_e}/\mu_{n_e}$ ) parameters show no correlation.

## SI Text 2. MATLAB code

### Fitting File 1: "HEDA Fit"

```
%% Initialize global variables for fitting

global epsilonNC epsilonSolvent pathLength
epsilonNC=4.0; % Dielectric background constant of nanocrystal
(ITO=4)
epsilonSolvent=1.505^2; % T E Host/solvent Dielectric Consta
lowFreqCutoff=2000; % Low frequency cutoff for fitting in wavenumbers
hiFreqCutoff=10000; % High frequency cutoff for fitting in wavenumbers
pathLength=0.05; %Pathlength in cm

%% Load data
% The data should be in a text file named "spectrum_to_fit" and they should
% be formatted so that wavenumbers are in the first column and absorption
% values are in the second column
sample_name='sg1_20nm_Dil5'
spectrum=dlmread('sg1_20nm_Dil5.txt','\t',2,0);
wavenumbers=spectrum(:,1); %load regular frequency values in cm-1
absorption=spectrum(:,2); %load absorption values

% set fitting window
%set limits of fitting and grab indices
limits=find(wavenumbers>lowFreqCutoff&wavenumbers<hiFreqCutoff);
reducedFrequency=wavenumbers(limits);
reducedAbsorption=absorption(limits);%extract frequencies

%% Drude Model (frequency independent damping)

global n_point p

n_point= 41
% p -- a vector of pre parameters:
% p(1) -- radius stdev
% p(2) -- radius mu_r
% p(3) -- volume fraction

p = [0.662 9.558 6.44E-05];

%% fitting
options=optimoptions('lsqcurvefit','Algorithm','trust-region-
reflective','MaxFunEvals',1e20,'MaxIter',5e10,'TolFun',1e-14,'TolX',1e-15);
op.Display='on';
op.Plot=0;
op.ErrorsUnknown=1; %set this to 1 if measurement uncertainties
are unknown
op.MaxFunEvals=1e20;
op.TolX=1e-20; %Smallest step tolerance
op.TolFun=1e-20;
op.MaxIter=1e20; %Maximum iterations possible
```

```
          % ne    ne_stdev    dep
LowerBound = [1*10^24 1*10^23 1*10^24];
initialGuess= [3.5*10^26 1*10^26 7*10^26]
UpperBound = [2*10^27 1*10^27 1*10^27];
disp('$$$$$$$$$$$$$$$$$$$$$$$$$$$$$$$$$$$$$$$$$$$$$$$$$$$$$$$$')
disp('Broadened Drude')

paramsITO_ed=lsqcurvefit(@drude_broad_sol,initialGuess,reducedFrequency,reduc
edAbsorption,LowerBound,UpperBound,options);
```

## Fitting File 2: "drude\_broad\_sol"

```
function A=drude_broad_sol(a,omega)
%This function is used to calculate the plasmonic absorbance spectrum of an
ensemble of NCs
%It uses a 2 dimensional probability distribution function and sums the
normalized absorbance spectrum
%of each element of the PDF which is distributed in damping constant and
plasma frequency.
% Input variables
%     omega -- frequency variable in cm^-1
%     a -- a vector of fit parameters:
%     a(1) -- plasma frequency expectation value cm^-1 mu_wp
(omega_p)
%     a(2) -- damping constant expectation value cm^-1 mu_gamma
%     a(3) -- plasma frequency broadening constant cm^-1 sigma_wp
%     a(4) -- damping constant broadening constant cm^-1 sigma_gamma
%
%     p -- a vector of fit parameters:
%     p(1) -- shape mu_shape
%     p(2) -- radius mu_r
%     p(3) -- volume fraction
% Output variable
% A -- absorbance of the layer

global epsilonNC epsilonSolvent pathLength n_point lower_limit upper_limit p
vol_frac=p(3);
ravg=p(2);
rstdev=p(1);

l=17;
r_range=(linspace(ravg-3*rstdev,ravg+3*rstdev,n_point))';
ne_range=linspace(a(1)-3*a(2),a(1)+3*a(2),n_point); %a(1)-3*a(2)
r_pdf=normpdf(r_range,ravg,rstdev)';
ne_pdf=normpdf(ne_range,a(1),a(2));
dep=a(3)*10^-27; %ne_range/(ne_ideal); %ne_range/(ne_ideal)*(r_range-
0.5).^3./(r_range.^3)%vf non-dead-zone
abs_ensemble=zeros(length(omega),1);
PD=zeros(n_point,n_point);
T_PD=0;
V=0;
delr=(r_range(2)-r_range(1));
delne=(ne_range(2)-ne_range(1));

gamma=(( (1.055*10^-34)*(3*pi^2)^(1/3)/(0.4*9.11*10^-
31*3*10^10*2*pi)).*ne_range.^(1/3).*(1./(4/3*r_range*dep^(1/3)*10^-
9)+1/(1*10^-9)));
omega_P=((ne_range)*(1.6*10^-19)^2/((8.85*10^-12)*(0.4*9.11*10^-
31))).^(1/2)/(3*10^10)/2/pi;
omega_s=((10^23)*(1.6*10^-19)^2/((8.85*10^-12)*(0.4*9.11*10^-
31))).^(1/2)/(3*10^10)/2/pi;

for i = 1:n_point
for j =1:n_point
```

```

        eshell=epsilonNC-
omega_s^2./(omega.^2+1i*omega.*(gamma(i,j)));    %scaled units on gamma
        epsilonParticle=epsilonNC-
omega_P(i)^2./(omega.^2+1i*omega.*(gamma(i,j)));    %scaled units on gamma

e_eff_particle=eshell.*((epsilonParticle+2*eshell)+2*dep*(epsilonParticle-
eshell))./((epsilonParticle+2*eshell)-dep*(epsilonParticle-eshell));

sigA=4*pi*r_range(j)^3*2*pi*omega*sqrt(epsilonSolvent).*imag((
e_eff_particle-epsilonSolvent)./( e_eff_particle+2*epsilonSolvent));
        abs1=sigA;
        absc(i,j,:)=abs1;
        PD(i,j)=delr*delne*r_pdf(j)*ne_pdf(i);
        abs_ensemble=abs_ensemble+PD(i,j)*abs1; % adding onto the
total abs
        T_PD=T_PD+PD(i,j);           %finding the total area of PDF for
normalizing
        V=V+4/3*pi()*r_range(j)^3*PD(i,j);
        end
        end
T_PD;
A=abs_ensemble*vol_frac*pathLength/(V*log(10)*T_PD);
end

```

## Simulation File: "Simulation"

```
epsilonNC=4.0;
epsilonSolvent=1.505^2;
l=17;
pathLength=0.05;
omega=linspace(100,10000,2500)';

%Sample=["sg0_20" "sg1_20" "sg3_20" "sg4p5_20" "sg6_20"
"sg8_20"];
ne0=[7.4E25 3.21E26 6.31E26 9.18E26 1.02E27
1.12E27];
rNC0=[8.909 9.558 9.31 9.228 8.804 8.718];
dep0=[0.5087 0.6719 0.8107 0.9513 0.9747 0.9745];

%Sample=["sg5_5" "sg5_7" "sg5_15" "sg5_10" "sg5_18"
"sg5_20"];
ne1=[7.75E26 8.86E26 7.68E26 10.2E26 8.93E26
8.64E26];
rNC1=[3.307 3.936 5.834 5.956 7.008
9.461];
dep1=[0.4747 0.7238 0.7888 0.9254 0.9299
0.9479];

Peaks=zeros(6,1);
Locations=zeros(6,1);
Spectra=zeros(length(omega),7);
Spectra(:,7)=omega;

for i=1:6
V=4/3*pi()*rNC^3;
gamma=((1.055*10^-34)*(3*pi^2)^(1/3)/(0.4*9.11*10^-
31*3*10^10*2*pi)).*ne.^(1/3).*(1./(4/3*rNC*dep^(1/3)*10^-9)+1/(1*10^-9));
omega_P=((ne)*(1.6*10^-19)^2/((8.85*10^-12)*(0.4*9.11*10^-
31))).^(1/2)/(3*10^10)/2/pi;
omega_s=((10^23)*(1.6*10^-19)^2/((8.85*10^-12)*(0.4*9.11*10^-
31))).^(1/2)/(3*10^10)/2/pi;
eshell=epsilonNC-omega_s^2./(omega.^2+1*sqrt(-1)*omega.*(gamma));
epsilonParticle=epsilonNC-omega_P^2./(omega.^2+1*sqrt(-1)*omega.*(gamma));
e_eff_particle=eshell.*((epsilonParticle+2*eshell)+2*dep*(epsilonParticle-
eshell))./((epsilonParticle+2*eshell)-dep*(epsilonParticle-eshell));
sigA=(4*pi*rNC^3*2*pi*omega*sqrt(epsilonSolvent).*imag((e_eff_particle-
epsilonSolvent)./(e_eff_particle+2*epsilonSolvent)))/(V*10^4);

[Peak,Location]=max(sigA);
Position=omega(Location);
Peaks(i,:)=Peak;
Locations(i,:)=Position;
Spectra(:,i)=sigA;
figure
plot(omega,sigA,'b')
end
```